

Organ-Aware Attention Improves CT Triage and Classification

Lavsen Dahal
Duke University
Durham, NC, USA
lavsen.dahal@duke.edu

Yubraj Bhandari
Duke University
Durham, NC, USA
yubraj.bhandari@duke.edu

Geoffrey D. Rubin
University of Arizona
Tucson, AZ, USA
grubin@arizona.edu

Joseph Y. Lo
Duke University
Durham, NC, USA
joseph.lo@duke.edu

Abstract

There is an urgent need for triage and classification of high-volume medical imaging modalities such as computed tomography (CT), which can improve patient care and mitigate radiologist burnout. Study-level CT triage requires calibrated predictions with localized evidence; however, off-the-shelf Vision-Language Models (VLM) struggle with 3D anatomy, protocol shifts, and noisy report supervision. This study used the two largest publicly available chest CT datasets—CT-RATE and RADCHEST-CT (held-out external test set). Our carefully tuned supervised baseline (instantiated as a simple Global Average Pooling head) establishes a new supervised state of the art, surpassing all reported linear-probe VLMs. Building on this baseline, we present ORACLE-CT, an encoder-agnostic, organ-aware head that pairs Organ-Masked Attention (mask-restricted, per-organ pooling that yields spatial evidence) with Organ-Scalar Fusion (lightweight fusion of normalized volume and mean-HU cues). In the chest setting, ORACLE-CT’s masked attention model achieves AUROC 0.86 on CT-RATE; in the abdomen setting, on MERLIN (30 findings), our supervised baseline exceeds a reproduced zero-shot VLM baseline obtained by running publicly released weights through our pipeline, and adding masked attention plus scalar fusion further improves performance to AUROC 0.85. Together, these results deliver state-of-the-art supervised classification performance across both chest and abdomen CT under a unified evaluation protocol. The source code is available at <https://github.com/lavsendahal/oracle-ct>.

1. Introduction

Computed tomography (CT) is among the most widely used imaging modalities, with over 90M scans performed

in the United States in 2023 [26, 35]. Chest and abdomen–pelvis studies comprise over half of these exams, and volumes continue to rise while the radiologist workforce does not [45], increasing backlog, and reducing time per case [27, 41]. As each CT dataset is a large, 3D volume, radiologists must interrogate hundreds of slices per study across heterogeneous scanners and protocols (non-contrast/contrast, arterial/venous phases), making the detection and classification of disease time-consuming and error-prone [10, 18, 30].

At the same time, computer vision has advanced rapidly. Convolutional neural networks (CNNs) and self-supervised Vision Transformers (ViT) (e.g., ResNet, Inception, DiNOv3) [14, 22, 34, 37], have propelled image classification, while accurate multi-organ 3D segmentation is now accessible via open-source or commercial tools [7, 33, 36, 44]. In parallel, large language models (LLMs) [4, 12, 38, 40] reduce annotation burden by parsing radiology text reports into structured findings [11, 19, 25, 29], enabling large-scale supervised CT training.

Vision–language models (VLM) excel on natural images via large-scale image–text contrastive pretraining, yielding transferable features and strong zero-/few-shot generalization [28]. But directly porting this recipe to CT exposes three mismatches: (i) **modality/geometry**—3D CT volumes with quantitative, physically calibrated Hounsfield Units (HU) with protocol-dependent contrast rather than 2D RGB photos; (ii) **supervision**—radiology reports are long and heterogeneous, interleaving positive and negative findings, prior comparisons, and recommendations, vs. short object-centric captions; and (iii) **alignment**—organ and finding-level evidence is weakly grounded in text and spatially sparse/uneven across slices. Consequently, contrastive objectives that work in natural images do not automatically yield reliable calibrated clinical behavior [21, 32,

42].

In response, CT-VLMs have taken two paths: **(A) Global** models align an entire study with its full report (e.g., CT-CLIP/CT-GLIP), which is convenient but coarse and prone to *implicit negatives*, reducing organ-level interpretability and stability [13, 21]. They also show strong *prompt sensitivity*, with zero-shot performance varying across near-equivalent phrasings—problematic for auditable triage [42]. **(B) Anatomy-aware** models (e.g. fVLM) add 3D masks and organ-wise text to mitigate misalignment and lift zero-shot AUCs [20, 32]. Yet across *both* families, core issues persist: sparse organ-finding-level grounding in reports, sensitivity to prompt wording and calibration choices [3, 42] that do not automatically yield reliable, well-calibrated behavior for clinical CT triage. This motivates a third path: a supervised, anatomy-guided pooling head that optimizes directly for CT labels. We adopt a *Multiple Instance Learning (MIL)* formulation: each organ group mask defines a bag of token/voxel instances; a small *unary* scorer assigns one scalar per instance and a *mask-restricted softmax* yields a permutation-invariant organ embedding for study-level classification. It is soft attention over sets [1, 8, 16, 24, 46, 47] using segmentation masks, while avoiding pairwise Q-K-V mixing used in Transformers [6, 40, 43].

Our approach. We introduce *ORACLE-CT* (ORgan-Aware Classification Engine for CT), which has two complementary pillars. *(i) Organ-masked softmax pooling (unary) with Organ-Scalar Fusion (OSF)*: for each organ, a unary scorer produces one scalar per local feature; we normalize *within the organ mask* and pool an organ embedding, then (optionally) append compact HU/volume scalars for classification. *(ii) An encoder-agnostic classification engine and fixed, auditable protocol*: any 2D/2.5D/3D backbone that outputs a feature lattice can be plugged in, while preprocessing, label maps, splits, calibration (temperatures/thresholds fixed on validation), and decision rules are held constant. This design yields calibrated operating points and *auditable* organ-weight maps; we treat these maps as supportive evidence rather than causal attributions [17]. As *ORACLE-CT* uses the same multi-organ masks as anatomy-aware VLMs, segmentation is a *shared, once-per-study* cost reusable across labels and models [7, 36, 44]. The key difference is *objective alignment*: we learn directly from CT disease labels rather than proxy text alignment, reducing exposure to modality and supervision gaps. We therefore report side-by-side with CT-VLM references using their strongest linear-probe or zero-shot results under our harmonized protocol [13, 20, 21, 32, 42], and we stage ablations from *Global Average Pooling (GAP)* to *global attention (mask-free)*, *organ-masked pooling*, and *masked+OSF* to quantify the incremental value of anatomy guidance.

Contributions.

- **Organ-masked softmax pooling for CT Triage.** A lightweight, encoder-agnostic pooling head that scores each local feature with a unary scalar and *normalizes within the organ mask*, yielding permutation-invariant organ embeddings and spatially localized weight maps suitable for auditing.
- **Organ-Scalar Fusion (OSF).** A minimal extension that appends compact, mask-derived scalars (e.g., normalized volume, mean HU, truncation flag) to the pooled organ embedding, improving numerous findings sensitive to size or density.
- **Encoder-agnostic benchmarking protocol.** A single modular engine compares diverse 2.5D and 3D backbones under fixed preprocessing, label maps, splits, schedules, and calibration—enabling rigorous GAP vs. global attention vs. masked attention vs. masked attention + OSF comparisons.
- **Calibrated supervised SoTA.** With fixed preprocessing, splits, and calibration, *ORACLE-CT* establishes supervised SoTA on CT-RATE and MERLIN, outperforming prior supervised baselines and competitive linear-probe CT-VLMs.

2. Related Work

Early supervised baselines established feasibility at scale: a single-institution study on ~36k chest CTs reported AUROC 0.77 over 83 findings and released *Rad-ChestCT* [9]. Consistent with prior work, *diffuse* disease reliably outperform *focal* lesions across organs—lungs (effusion/emphysema vs. nodules), liver (steatosis/biliary dilation vs. lesions/calcifications), and kidneys (stones/atrophy vs. small lesions/cysts) [39]. *CT-RATE* then introduced paired 3D CT-report supervision; its VocabFine reached AUROC 0.756 (internal) and 0.650 (external) [13]. Anatomy-aware CT-VLMs further improved metrics: *fVLM* achieved 0.780 (internal) and 0.646 (external) [32], while segmentation-guided variants (e.g., *SegVL*) report 0.811 (internal) and 0.716 (external) [15]. *Uniferum* unifies classification and segmentation signals and reports AUROC 0.83 on *CT-RATE* [20]. Most recently, *COLIPRI* conducted an extensive ablation of contrastive pretraining, report-generation, and masked-image modeling objectives and reported the strongest *linear-probe* baselines to date: AUROC 84.15 on *CT-RATE* and 72.66 on *Rad-ChestCT* with frozen encoders. Notably, their zero-shot performance is highly prompt-sensitive, brief “short” diagnostic prompts underperform relative to “native” report-style prompts [42]. Concurrently, pan-organ CT-VLMs trained at biobank scale have appeared: *Percival* pretrains contrastively on > 400k CT-report pairs spanning thorax/abdomen/pelvis and yields strong frozen-encoder classifiers (respiratory mean AUROC \approx 0.73; cardiovascular \approx 0.76 with external cardiomegaly

Table 1. Illustrative backbones used in our experiments. The aggregation head is identical across all.

Backbone (example)	Feature substrate
DINOv3 [34]	Token lattice (2D/2.5D)
MedSigLIP [48]	Token lattice (2D/2.5D)
I3D-ResNet-121 [5, 14]	Voxel lattice (3D)
MedNeXt-3D [23, 31]	Voxel lattice (3D)
CT-Net [9]	Voxel lattice (3D)

0.83 on CT-RATE dataset), with variable but positive gains across abdominal/genitourinary categories [2].

Abdomen CT introduces multi-phase protocols and long-tail labels. Recent CT-VLMs (e.g., MERLIN, CT-GLIP) report competitive zero-shot transfer, but supervised and anatomy-aware baselines under fixed protocols remain scarce [3, 21]. ORACLE-CT fills this gap: an encoder-agnostic head that performs organ-restricted softmax pooling with optional Organ-Scalar Fusion, trained end-to-end in a fixed, auditable pipeline and evaluated side-by-side with GAP, global attention, and masked variants introduced next.

3. Method: ORACLE-CT

3.1. Problem Setup

A CT study is a 3D volume $X \in \mathbb{R}^{D \times H \times W}$ (axial slices D , height H , width W). We consider a **multi-label** setting with L study-level disease labels. Ground-truth targets are $y \in \{0, 1, -1\}^L$, where -1 denotes missing/unknown labels, we predict calibrated label probabilities $\hat{\mathbf{p}} \in [0, 1]^L$. An encoder E_θ extracts local features from X , and an aggregation head A_ϕ maps them to logits $z \in \mathbb{R}^L$:

$$z = A_\phi(E_\theta(X)), \quad \hat{\mathbf{p}} = \text{sigmoid}(z) \in [0, 1]^L.$$

3.2. Encoders as Feature Adapters

We treat the encoder as a *feature adapter* that maps a CT volume to a spatial lattice of local features. Let Ω be the index set of the encoder’s final feature lattice and let $\{u_i\}_{i \in \Omega}$ with $u_i \in \mathbb{R}^d$ denote the local features consumed by our aggregation head. Our contribution lies in the aggregation schemes; the head operates only on $\{u_i\}$ and is therefore **encoder-agnostic**—any backbone that yields a feature lattice can be plugged in.

We consider two common substrates (others are compatible): (i) a *token lattice* produced by 2.5D transformers (after dropping CLS/register tokens), and (ii) a *voxel lattice* produced by native 3D networks as shown in Table 1. We write $i \in \Omega$ for a lattice location (token or voxel) and flatten its coordinates for brevity.

3.3. From Feature Lattices to Aggregation Heads

Given an encoder that yields a lattice of local features $\{u_i\}_{i \in \Omega}$, we compare four *encoder-agnostic* heads in a staged ladder to isolate content weighting and anatomy priors (Fig. 1): (i) **GAP**—uniform averaging with a linear classifier (Eq. 1); (ii) **global attention(mask-free, unary)**—a scalar score per location with softmax over Ω (Eqs. 2–3); (iii) **organ-masked pooling**—the same operator but softmax normalized *within* each organ’s support, followed by per-organ classification (Eqs. 4–6); and (iv) **organ-masked + OSF**—augmenting the pooled organ feature with compact mask-derived scalars (volume, mean HU, truncation) before classification (Eq. 7).

3.3.1. Mask-free Heads

Global Average Pooling (GAP). Given $\{u_i \in \mathbb{R}^d\}_{i \in \Omega}$, we form a uniform average and classify:

$$h = \frac{1}{|\Omega|} \sum_{i \in \Omega} u_i \in \mathbb{R}^d, \quad z = W^{\text{global}} h + b^{\text{global}} \in \mathbb{R}^L. \quad (1)$$

Here $W^{\text{global}} \in \mathbb{R}^{L \times d}$ and $b^{\text{global}} \in \mathbb{R}^L$. GAP is *feature-only*, scales linearly in $|\Omega|$, is invariant to lattice density, and serves as our supervised baseline for the **multi-label** setting.

Global Attention (mask-free, content-weighted). To move beyond uniform pooling, we assign a learned weight to each location using a *unary* scorer (no Q/K/V), then softmax over the whole lattice:

$$\alpha_i = s_{\text{glob}}(u_i), \quad w_i = \frac{\exp(\alpha_i/\tau)}{\sum_{j \in \Omega} \exp(\alpha_j/\tau)}, \quad \tau > 0, \quad (2)$$

This is classic *soft attention pooling* over the full lattice (unary scoring + softmax over Ω) as in [1, 24, 46], and unlike Transformer style Q–K–V feature mixing [40, 43].

$$h = \sum_{i \in \Omega} w_i u_i \in \mathbb{R}^d, \quad z = W^{\text{global}} h + b^{\text{global}} \in \mathbb{R}^L. \quad (3)$$

Here $s_{\text{glob}} : \mathbb{R}^d \rightarrow \mathbb{R}$ is a tiny per-location map (e.g., $\text{Linear}(d \rightarrow 1)$ for tokens or $1 \times 1 \times 1$ Conv3D for voxels), and the weights satisfy $w_i \geq 0$ and $\sum_i w_i = 1$. Compared to GAP, which averages uniformly, global attention *learns* a content-weighted mixture that can emphasize salient regions while remaining mask-free and encoder-agnostic. The head adds only $\mathcal{O}(|\Omega|)$ compute and reduces to GAP when all α_i are equal (or as $\tau \rightarrow \infty$).

3.3.2. Organ-aware Heads

Mask-free pooling (GAP/Global Attention) can overweight off-organ cues. We therefore add an *anatomy prior*

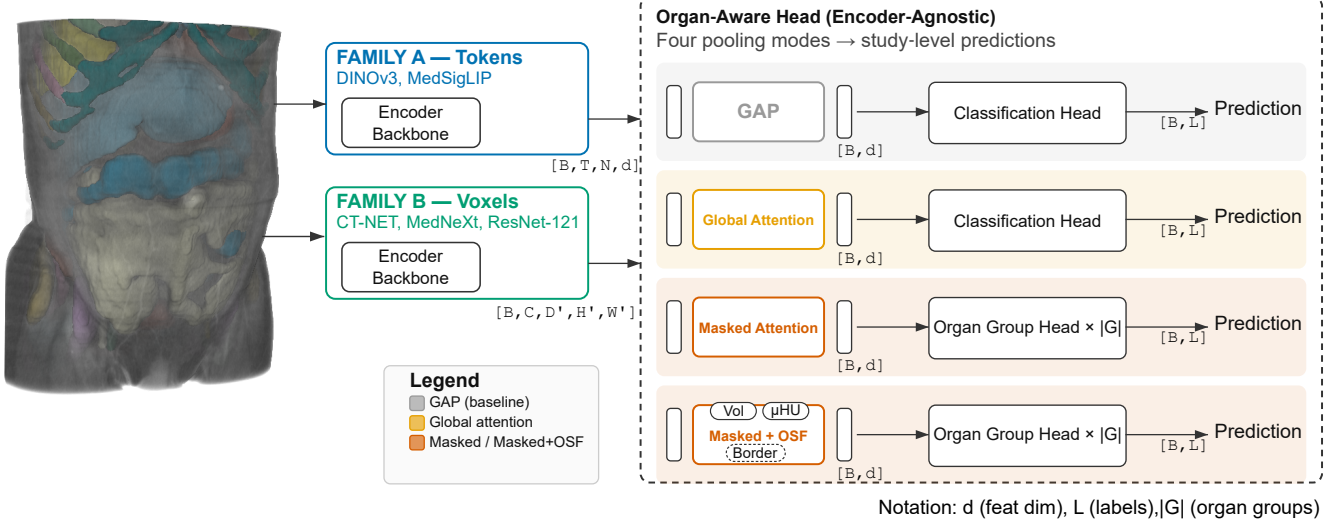


Figure 1. **ORACLE-CT overview.** Two encoder families feed a shared organ-aware head: *Family A* 2.5D token towers (DINOv3, MedSigLIP) and *Family B* native 3D trunks (CT-NET, I3D-ResNet-121, MedNeXt-3D). The head supports four pooling modes: *GAP*, *Global attention* (mask-free unary softmax over the lattice), *Masked attention* (softmax restricted to organ masks; one head per organ group plus an *other* head), and *Masked + OSF* (append organ volume/HU/border scalars). Outputs are study-level predictions. Organ merges and label groups are in Appendix Tables 7 and 8.

that localizes evidence to clinically meaningful regions while keeping the encoder generic. Concretely, raw segmentation classes \mathcal{C} are merged into a small set of *organ groups* \mathcal{O} (e.g., all lung lobes \rightarrow lungs; left/right kidneys \rightarrow kidneys; stomach/Vesophagus \rightarrow stomach/esophagus). For each raw class $c \in \mathcal{C}$, let $S_c \in \{0, 1\}^{D \times H \times W}$ denote its binary segmentation mask on the native CT grid (1 inside class c , 0 otherwise). Let $\pi : \mathcal{C} \rightarrow \mathcal{O}$ map classes to groups and define $M_o = \bigvee_{c: \pi(c)=o} S_c$ on the native CT grid. We dilate M_o by r_o mm (metric space) to absorb boundary uncertainty, then resample to the encoder lattice Ω (tokens or voxels) to obtain indicators $m_{o,i} \in \{0, 1\}$ and support $\Omega_o = \{i \in \Omega : m_{o,i} = 1\}$.

Each study-level label $\ell \in \mathcal{L}$ is *anchored* to exactly one group via a fixed map $\kappa : \mathcal{L} \rightarrow \mathcal{O} \cup \{\text{other}\}$, yielding disjoint label sets $\{\mathcal{L}_o\}_{o \in \mathcal{O}}$ and $\mathcal{L}_{\text{other}}$. Unlike mask-free heads (single global classifier for all L labels), the organ-aware design uses a *bank of heads*: one per group o for \mathcal{L}_o , plus an *other* head for labels without a stable segmentation region. Organ groups and dilation radii r_o (mm) are defined in Appendix Tables 7 and 8. This procedure is encoder-agnostic; only mask-to-lattice alignment differs across backbones.

Organ-masked attention. Given $\{u_i\}_{i \in \Omega}$ and masks $m_{o,i}$, each organ group o applies a lightweight *per-group unary scorer* $s_o : \mathbb{R}^d \rightarrow \mathbb{R}$ (Linear($d \rightarrow 1$) on tokens or $1 \times 1 \times 1$ Conv3D on voxels; no Q/K/V, $\mathcal{O}(|\Omega|)$ cost), a temperature $\tau_o > 0$, and optional inside/outside priors

$$(\beta_o^{\text{in}}, \beta_o^{\text{out}}):$$

$$\tilde{\alpha}_{o,i} = s_o(u_i) + \beta_o^{\text{in}} m_{o,i} + \beta_o^{\text{out}} (1 - m_{o,i}). \quad (4)$$

Attention is *normalized within* the organ support via a masked softmax,

$$w_{o,i} = \frac{\exp(\tilde{\alpha}_{o,i}/\tau_o) m_{o,i}}{\sum_{j \in \Omega_o} \exp(\tilde{\alpha}_{o,j}/\tau_o) + \varepsilon}, \quad \varepsilon > 0, \quad (5)$$

followed by per-organ pooling and classification:

$$h_o = \sum_{i \in \Omega_o} w_{o,i} u_i, \quad z_o = W^{(o)} h_o + b^{(o)} \in \mathbb{R}^{|\mathcal{L}_o|}. \quad (6)$$

If Ω_o is empty at the pooling resolution, we fall back to uniform pooling over Ω for that organ. Labels in $\mathcal{L}_{\text{other}}$ use the mask-free global attention head.

Organ-Scalar Fusion (Masked+OSF). We extend the organ-masked head by adding a few simple, mask-derived scalars per organ and then predicting with a small head.

For each organ o , we extract three mask-derived scalars: (i) a *normalized volume* v_o (z-scored over the training set), (ii) a *mean HU* $\bar{\mu}_o^{\text{HU}}$ (after standard clipping, then z-scored), and (iii) a binary *border-contact flag* $b_o \in \{0, 1\}$ indicating whether the (dilated) mask touches the scan field-of-view boundary. We collect these as $u_o = [v_o, \bar{\mu}_o^{\text{HU}}, b_o]$ (additional clinically useful scalars can be appended).

From masked attention we already have a per-organ spatial feature $h_o \in \mathbb{R}^d$. If the organ is flagged as truncated ($b_o=1$), we *softly down-weight* h_o by a single learned gate

(one scalar per organ group) so the model relies a bit less on potentially biased spatial evidence. We then *append* the scalars to the (possibly down-weighted) feature and predict the organ’s labels with a small head:

$$\begin{aligned}\hat{h}_o &= [h_o; u_o] \in \mathbb{R}^{d+k}, \\ z_o &= W^{(o)}\hat{h}_o + b^{(o)} \in \mathbb{R}^{|\mathcal{L}_o|}.\end{aligned}\quad (7)$$

Here $W^{(o)} \in \mathbb{R}^{|\mathcal{L}_o| \times (d+k)}$ and $b^{(o)} \in \mathbb{R}^{|\mathcal{L}_o|}$. When $k=0$ (no scalars), (7) reduces exactly to the masked-attention classifier.

Implementation details. A complete implementation on the DINOv3 token backbone, covering 3D volume to 2D slices framing, token–lattice formation, mask projection/alignment, scalar computation and normalization is provided in Appendix Section 6.1

3.4. Training Objective and Calibration

Training loss. We minimize a per-label Binary Cross Entropy (BCE) with-logits loss, normalized by the total effective label weight for stable scale. Observed labels contribute with unit weight. Labels marked as missing are ignored for an initial burn-in of n_{burn} epochs and are then included as weak negatives with a linearly increasing weight over n_{ramp} epochs up to a small cap w_{max} . This schedule avoids early over-penalizing uncertain supervision and improves stability, calibration, and recall. Class imbalance is handled via conservative positive-class reweighting.

Training & evaluation. All models share the same pre-processing, splits, loss, calibration, and fixed decision-threshold protocol—varying only the aggregation mode (GAP, Global, Masked, Masked+OSF) and the encoder family (token vs. voxel). Model selection uses validation loss. Per-label temperature scaling and F1-optimal thresholds are fit on the validation set and then frozen for test and external evaluation. Metrics exclude missing targets (-1) from denominators, following prior work [3]. We report macro AUROC, AUPRC, F1, and Balanced Accuracy and per class AUROC/AUPRC. Complete hyperparameters appear in Appendix Table 9.

4. Experiments and Results

4.1. Datasets and Splits

Chest datasets. *Internal:* CT–RATE—18 study-level findings with official patient-disjoint splits; we follow the released label map, remove non-chest volumes as in prior work [20], and report final counts in Table 2. For organ-aware pooling, fine-grained masks are collapsed into a small set of chest organ groups that define pooling regions (Appendix Table 7). *External:* RAD–ChestCT—public chest

CT test set [9] harmonized to the CT–RATE 16-label protocol using the same mapping as prior work [13] (e.g., *Classification* = $\max(\text{arterial wall}, \text{coronary})$; *Mosaic attenuation* absent and excluded). External evaluation is strictly transferred: per-label temperature scaling and F1-optimal thresholds are fit on CT–RATE validation and applied unchanged to RAD–ChestCT; organ-mask merges and dilation radii mirror CT–RATE.

Abdomen dataset - MERLIN Large abdomen–focused corpus with 30 study-level labels as positive, negative or missing [3]. We use the released patient-disjoint splits (counts in Table 2). For organ grouping, TotalSegmentator classes [44] are merged into 13 organ groups (with fixed metric-space dilations r_o in mm), plus an additional category *other*. Here, *other* collects labels that cannot be assigned to any organ group because (i) the relevant anatomy has no corresponding segmentation class, or (ii) the finding is not well localized (e.g., diffuse/systemic or protocol/device related). The full, fixed mapping of labels to organ groups (including which labels fall under *other*) is provided in Appendix Table 8.

Preprocessing and Augmentations- Unless noted, intensities are clipped to $[-1000, 1000]$ HU and min–max normalized to $[0, 1]$ dataset-specific voxel spacing and volume dimensions are listed in Table 2. CT–RATE uses random in-plane rotations and per-axis flips. MERLIN uses small 3D affine transforms (in-plane rotation, translation, scaling), gamma jitter, and low-variance noise, with left–right, anterior–posterior, and crano–caudal flips disabled to preserve laterality (e.g., spleen left, liver right).

4.2. Chest CT - Classification Results

Supervised GAP baselines (SOTA comparison). On CT–RATE, our supervised GAP setup already achieves **state-of-the-art** results within our fixed protocol and reported against CT–VLM linear-probe references: **Inflated ResNet–121 (GAP)** leads with **AUROC 85.74 / AUPRC 61.73 / F1 59.91 / BA 76.12**, with DINOv3 and MedNeXt close behind. Under external shift (RAD–ChestCT), the same GAP baseline remains strong (**AUROC 76.45 / F1 51.80**), reinforcing our thesis that calibrated, anatomy-aware supervision—without large-scale Vision Language pretraining—already delivers competitive triage performance. We report full internal/external results and fair VLM linear-probe comparisons in Table 3. Per class AUROC/AUPRC scores are presented in Appendix Figure 6.

Segmentation-guided upgrade (masked attention). Applying our *organ–masked attention* head atop the best supervised backbone (Inflated ResNet–121) yields $\Delta\text{AUROC} = +0.42$ and $\Delta\text{F1} = +0.47$ on CT–RATE vs. its GAP baseline, and matches AUROC with a small F1 gain on RAD–ChestCT (Table 4). We run the full four–mode ablation (GAP \rightarrow Global \rightarrow Masked \rightarrow Masked+OSF) on

Table 2. **Datasets and I/O geometry.** Organ group counts list only *masked* groups (excluding *other*); full merges and per-group dilations are in Appendix Table 7 and Table 8). All volumes are clipped to $[-1000, 1000]$ and normalized to $[0, 1]$ (Sec. 4.1).

Dataset	Train	Val	Test	Organ groups (masked)	Resampled Spacing (mm)	Shape
CT-RATE	43,738	3,409	3,040	4 (+other)	$1.5 \times 1.5 \times 1.5$	224^3
MERLIN	15,175	5,018	5,082	13 (+other)	$3 \times 1.5 \times 1.5$	$160 \times 224 \times 224$
RAD-ChestCT (ext.)	—	—	3630	4 (+other)	$1.5 \times 1.5 \times 1.5$	224^3

Table 3. **Chest results on CT-RATE (internal) and RAD-ChestCT (external).** Prior VLM baselines are taken *as reported* by [42]—their strongest *linear-probe* (frozen encoder + linear head) results. In contrast, we evaluate *supervised* encoders (GAP shown) under one fixed, auditable protocol. Per-label temperatures/thresholds are fit once on CT-RATE validation and applied unchanged to CT-RATE test and to RAD-ChestCT, which we harmonize to the CT-RATE 16-label map. For comparability with [42], AUROC/AUPRC are reported as percentages in this table only.

Method	CT-RATE (internal test)				RAD-ChestCT (external)			
	AUROC \uparrow	AUPRC \uparrow	F1 \uparrow	BA \uparrow	AUROC \uparrow	AUPRC \uparrow	F1 \uparrow	BA \uparrow
<i>Prior work (VLM, linear-probe references)</i>								
CT-CLIP	61.21	25.96	34.49	57.66	54.05	28.77	39.08	52.65
CT-FM	82.14	53.54	55.56	73.51	68.49	42.41	47.55	61.95
Merlin	82.62	54.81	56.69	74.28	70.91	45.30	49.35	64.34
COLIPRI-C	84.15	57.41	57.99	74.99	72.66	48.86	51.31	65.17
<i>Ours (supervised GAP, backbone sweep)</i>								
CT-Net	79.59	49.32	51.04	71.61	68.14	42.30	44.30	61.61
MedSigLIP	83.61	58.17	56.24	73.93	74.44	50.40	47.76	65.80
MedNeXt-3D	84.41	58.37	57.76	75.75	72.87	48.39	48.42	65.86
DINOv3	84.52	59.17	57.24	74.30	76.25	52.59	50.11	66.33
Inflated ResNet-121	85.74	61.73	59.91	76.12	76.45	54.32	51.80	68.39

Table 4. **Segmentation-guided chest classification (AUROC).** ORACLE-CT applies organ-masked attention to the best GAP baseline (Inflated ResNet-121). CT-RATE protocol; RAD-ChestCT harmonized to 16 labels.

Method	CT-RATE	RAD-ChestCT
	AUROC \uparrow	AUROC \uparrow
fVLM	0.78	0.68
SegVL	0.81	0.72
Uniferum	0.83	—
Ours (ORACLE-CT)	0.86	0.76

MERLIN (abdomen; 13 organ groups), where fine-grained organ grouping particularly benefits our organ-aware design; chest uses only four groups, yet we still see targeted gains, notably for *hiatal hernia*. Chest results per class AUROC/AUPRC are in Appendix Figs. 7 and 8.

4.3. Abdomen CT Classification Results

Supervised vs. zero-shot on Merlin. Table 5 reports macro AUROC/AUPRC/F1/BA on the official *Merlin* test split.

As the released *Merlin* [3] weights do *not* ship with zero-shot prompts, we constructed class-wise positive and negative phrasings using a large language model, full list in Appendix Table 12) and ran zero-shot inference from the authors’ checkpoint for a fair comparison on the *full* test set (their reported results are on a class-balanced subset). Across all five encoders, our fully supervised models surpass the reproduced zero-shot baseline; the DINOv3 encoder is the best overall, absolute AUROC/AUPRC values are present in Appendix Figure 9.

Four aggregation modes on DINOv3. Table 6 shows both mask-based variants outperform GAP and global attention; *Masked+Scalar* is slightly better than masked attention (AUROC 0.85 vs 0.84; AUPRC 0.68 vs 0.66); with the improvements notably on size driven labels (*e.g.*, “-megaly”). As masked attention depends on segmentation quality, labels lacking reliable masks (*e.g.*, appendicitis, gallbladder pathology) can favor GAP, see class-wise trends in Fig. 2. To address this, Ablations Section 4.5 also evaluates bounding-box regions in place of masks.

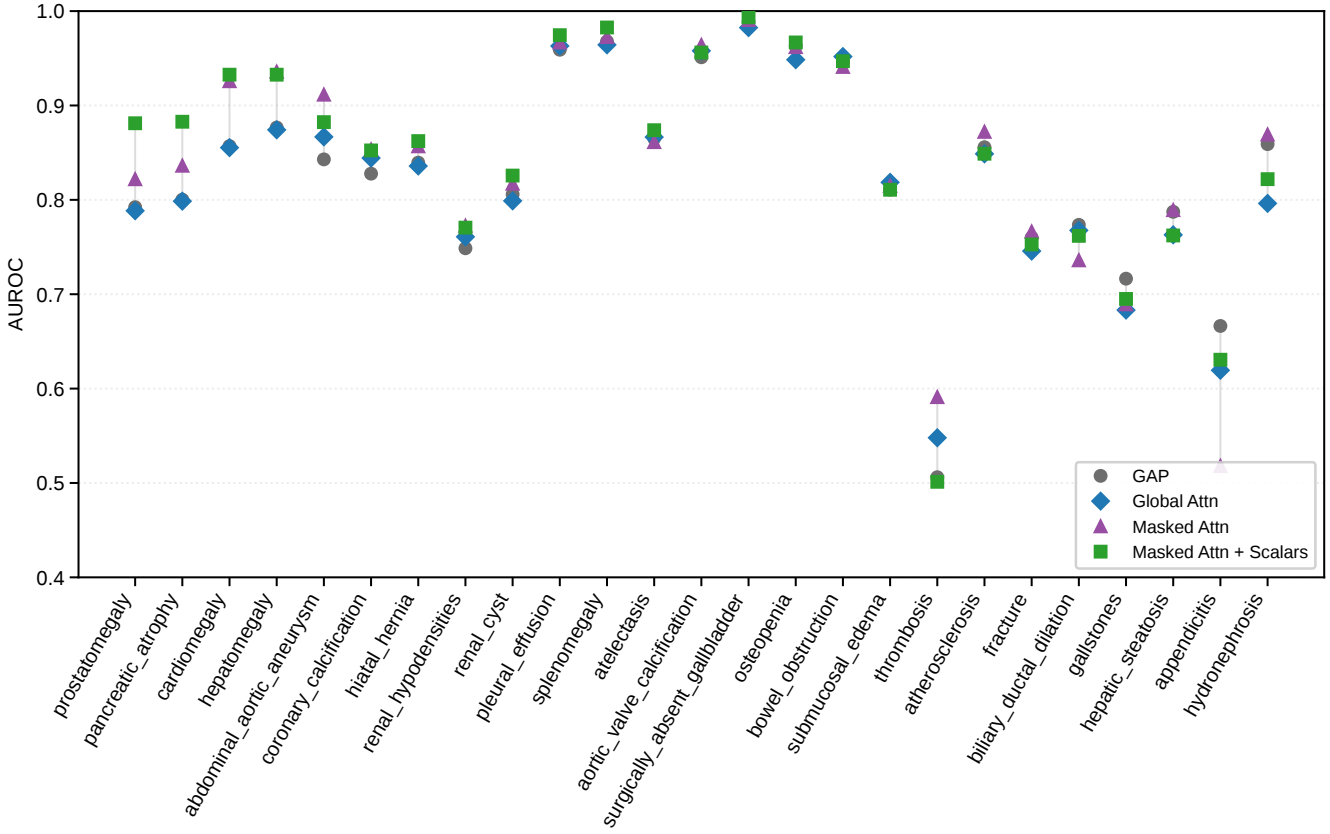


Figure 2. **MERLIN (abdomen), DINOV3: per-class AUROC across four aggregation modes.** We compare *GAP*, *Global attention* (mask-free), *Organ-masked attention*, and *Masked+OSF* (masked attention + organ scalars: mean HU, volume). Shown are the 25 mask-eligible classes (the 5 labels without stable organ masks are omitted). *Classes are sorted by the absolute AUROC gain of Masked+OSF over GAP.* Masked+OSF provides the most consistent improvements—especially for size/morphology-driven findings at the left—while organ-masked attention alone already lifts most organ-tied labels.

Table 5. **MERLIN test Results.** Top row: zero-shot baseline on the official MERLIN test set; original prompts are unavailable, so we re-created them (see Appendix Table 12). Rows below the rule: our supervised GAP baselines across five encoder backbones.

Method	AUROC \uparrow	AUPRC \uparrow	F1 \uparrow	BA \uparrow
Merlin Zero-Shot	0.72	0.50	0.47	0.64
Ours (CT-Net)	0.75	0.51	0.54	0.66
Ours (MedNeXt)	0.78	0.54	0.55	0.66
Ours (ResNet-121)	0.81	0.59	0.59	0.69
Ours (MedSigLip)	0.82	0.61	0.59	0.70
Ours (DINOV3)	0.83	0.64	0.63	0.72

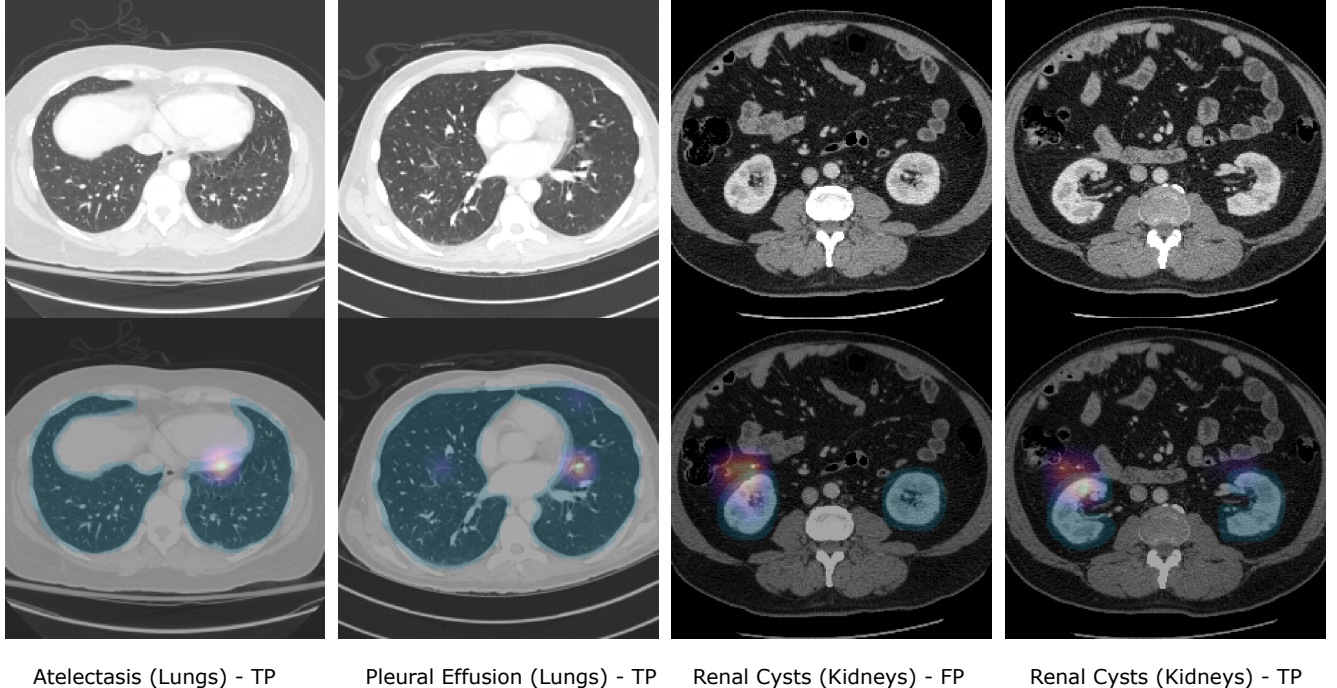
4.4. Qualitative Evidence

We visualize organ-masked attention for four MERLIN studies using DINOV3 in masked attention mode in Figure 3. Each column shows an axial CT slice (top) and an overlay (bottom) with the organ mask (cyan) and the masked-attention heatmap (magma). For lung findings (atelectasis,

Table 6. **MERLIN mode ablations (DINOV3).** Compare GAP, global attn, masked attn, and masked attn+scalar (+volume, HU, border-touch); mask-based modes beat GAP/global, with masked+scalar showing the best results.

DINOV3 Modes	AUROC \uparrow	AUPRC \uparrow	F1 \uparrow	BA \uparrow
GAP Baseline	0.83	0.64	0.63	0.72
Global Attn	0.83	0.63	0.63	0.73
Masked Attn	0.84	0.66	0.63	0.73
Masked Attn + OSF	0.85	0.68	0.66	0.74

pleural effusion), attention remains within the lungs. For renal cysts, the TP example shows kidney-confined evidence; the FP example also shows kidney-confined attention but an incorrect positive prediction. These maps depict organ-level pooling weights used to form the study-level logits—they provide anatomical context for where the model drew evidence, not pixel-accurate lesion segmentations or guarantees of correctness.



Atelectasis (Lungs) - TP

Pleural Effusion (Lungs) - TP

Renal Cysts (Kidneys) - FP

Renal Cysts (Kidneys) - TP

Figure 3. **Qualitative organ-masked attention on MERLIN.** Columns show four study examples: Atelectasis (TP), Pleural effusion (TP), Renal cyst (FP), and Renal cyst (TP). Top row: axial CT slice. Bottom row: organ mask (cyan) with masked-attention heatmap (magma). Maps depict *organ-level pooling weights* used for study-level classification (not lesion segmentation): they highlight where evidence within the organ contributed most to the logit. The FP renal-cyst case illustrates organ-faithful but misleading evidence.

4.5. Ablations

(A) Backbone freezing. All MERLIN results in Table 5 use *unfrozen* backbones. Comparing frozen vs. unfrozen backbone for DINOv3 and MedSigLIP, unfreezing consistently lifts AUROC/AUPRC, with larger and more uniform gains for DINOv3. Improvements concentrate on multi-organ, morphology/size-driven findings (e.g., “-megaly”, bowel obstruction, hydronephrosis, surgically absent gall-bladder), while highly localized or primarily HU-driven patterns show smaller or mixed changes. Net: unfreezing helps, but for focal targets most of the lift still comes from segmentation-guided attention (masked pooling + scalars). Per-class trends appear in Appendix Figure 11.

(B) Scalar fusion: HU-only vs. Volume-only. Fixing the region to the full *Segmentation Mask*, we compare HU-only vs. organ Volume-only fusion (both against the same GAP baseline). Volume tends to help size/morphology findings (e.g. *cardiomegaly*, *hepatomegaly*, *splenomegaly*, *pancreatic atrophy*), while HU favors intensity/density patterns (e.g. calcifications, thrombosis). Full per-class heatmaps are in Appendix Figure 12.

(C) Mask region: Segmentation Mask vs. Bounding Box. Masked pooling and OSF depend on segmentation; gains scale with region *fidelity* and *footprint*. We therefore compare using the full *Mask* vs. a tight *Bounding Box* as

the aggregation region. Both generally beat GAP, but the winner is class-dependent: for *appendicitis*, *Bounding Box* better captures peri-appendiceal context; for *biliary ductal dilation*, thin boundary-adjacent ducts benefit from periportal context. *Rule of thumb:* use *Bounding Box* for small/tubular or boundary-adjacent targets; use *Mask* for diffuse within-organ signals; otherwise choose by validation. Per-class heatmaps (AUROC/AUPRC) are in Appendix Figure 13.

5. Limitations and Future Work

Limitations. Our approach assumes reliable multi-organ segmentation; errors especially on small/tubular or truncated structures propagate to masked pooling/OSF. Masks are fixed pre-processing (no uncertainty or joint seg-class training). OSF uses uniform fusion of z-volume and mean HU, which can dilute focal signal. Attention maps aid audibility but are not guaranteed faithful. We did not fully tune backbones/schedules.

Future work. (i) *Disease-aware, gated scalars:* replace mean HU with robust summaries and enable sparse per-label fusion gates. (ii) *Faithfulness/robustness:* deletion-insertion curves, counterfactual mask edits, and calibration under masking. (iii) *Mask reliability & fallbacks:* estimate mask quality and marginalize/switch across mask,

padded box, or expanded regions. (iv) *Tuning & scaling*: systematic hyper-parameter sweeps, with parameter-efficient adapters.

6. Conclusion

We presented ORACLE-CT, a unified, supervised benchmark for CT triage that fixes data splits, label maps, and training protocol while varying two axes—aggregation (GAP, Global Attention, Masked, Masked+OSF) and backbone family (2.5D tokens vs. native 3D voxels). Across chest and abdomen, organ-masked pooling improves organized labels and calibration, with the masked+OSF head adding small, consistent gains for size-driven conditions. We will release code, configs, and checkpoints to enable comparisons and extensions. We hope this provides a practical baseline and a clear recipe for deploying calibrated, anatomy-aware CT triage systems.

References

- [1] Dzmitry Bahdanau, Kyunghyun Cho, and Yoshua Bengio. Neural machine translation by jointly learning to align and translate. *arXiv preprint arXiv:1409.0473*, 2014. [2](#) [3](#)
- [2] Cameron Beeche, Joonghyun Kim, Hamed Tavolinejad, Bingxin Zhao, Rakesh Sharma, Jeffrey Duda, James Gee, Farouk Dako, Anurag Verma, Colleen Morse, et al. A pan-organ vision-language model for generalizable 3d ct representations. *medRxiv*, 2025. [3](#)
- [3] Louis Blankemeier, Joseph Paul Cohen, Ashwin Kumar, Dave Van Veen, Syed Jamal Safdar Gardezi, Magdalini Paschali, Zhihong Chen, Jean-Benoit Delbrouck, Eduardo Reis, Cesar Truyts, et al. Merlin: A vision language foundation model for 3d computed tomography. *Research Square*, pages rs–3, 2024. [2](#) [3](#) [5](#) [6](#)
- [4] Tom Brown, Benjamin Mann, Nick Ryder, Melanie Subbiah, Jared D Kaplan, Prafulla Dhariwal, Arvind Neelakantan, Pranav Shyam, Girish Sastry, Amanda Askell, et al. Language models are few-shot learners. *Advances in neural information processing systems*, 33:1877–1901, 2020. [1](#)
- [5] Joao Carreira and Andrew Zisserman. Quo vadis, action recognition? a new model and the kinetics dataset. In *proceedings of the IEEE Conference on Computer Vision and Pattern Recognition*, pages 6299–6308, 2017. [3](#)
- [6] Bowen Cheng, Ishan Misra, Alexander G Schwing, Alexander Kirillov, and Rohit Girdhar. Masked-attention mask transformer for universal image segmentation. In *Proceedings of the IEEE/CVF conference on computer vision and pattern recognition*, pages 1290–1299, 2022. [2](#)
- [7] Lavsen Dahal, Mobina Ghojoghnejad, Liesbeth Vancoillie, Dhrubajyoti Ghosh, Yubraj Bhandari, David Kim, Fong Chi Ho, Fakrul Islam Tushar, Sheng Luo, Kyle J Lafata, et al. Xcat 3.0: A comprehensive library of personalized digital twins derived from ct scans. *Medical Image Analysis*, page 103636, 2025. [1](#) [2](#)
- [8] Thomas G Dietterich, Richard H Lathrop, and Tomás Lozano-Pérez. Solving the multiple instance problem with axis-parallel rectangles. *Artificial intelligence*, 89(1-2):31–71, 1997. [2](#)
- [9] Rachel Lea Draelos, David Dov, Maciej A Mazurowski, Joseph Y Lo, Ricardo Henao, Geoffrey D Rubin, and Lawrence Carin. Machine-learning-based multiple abnormality prediction with large-scale chest computed tomography volumes. *Medical image analysis*, 67:101857, 2021. [2](#) [3](#) [5](#)
- [10] Christopher S Evans, Rodney Arthur, Michael Kane, Fola Omofoye, Arlene E Chung, Elizabeth Moreton, and Carlton Moore. Incidental radiology findings on computed tomography studies in emergency department patients: a systematic review and meta-analysis. *Annals of Emergency Medicine*, 80(3):243–256, 2022. [1](#)
- [11] Michael E Garcia-Alcoser, Mobina GhojoghNejad, Fakrul Islam Tushar, David Kim, Kyle J Lafata, Geoffrey D Rubin, and Joseph Y Lo. Evaluating large language models for zero-shot disease labeling in ct radiology reports across organ systems. *arXiv preprint arXiv:2506.03259*, 2025. [1](#)
- [12] Google for Developers. Langextract — health ai developer foundations, 2025. Last updated 2025-07-30 UTC. [1](#)
- [13] Ibrahim Ethem Hamamci, Sezgin Er, Chenyu Wang, Furkan Almas, Ayse Gulnihan Simsek, Seval Nil Esirgun, Irem Doga, Omer Faruk Durugol, Weicheng Dai, Murong Xu, et al. Developing generalist foundation models from a multimodal dataset for 3d computed tomography. *arXiv preprint arXiv:2403.17834*, 2024. [2](#) [5](#)
- [14] Kaiming He, Xiangyu Zhang, Shaoqing Ren, and Jian Sun. Deep residual learning for image recognition. In *Proceedings of the IEEE conference on computer vision and pattern recognition*, pages 770–778, 2016. [1](#) [3](#)
- [15] Yuqi Hu, Xufang Luo, Zilong Wang, Dongsheng Li, and Lili Qiu. Segmentation helps understanding: Mask-infused vision-language pre-training for 3d medical images. [2](#)
- [16] Maximilian Ilse, Jakub Tomczak, and Max Welling. Attention-based deep multiple instance learning. In *International conference on machine learning*, pages 2127–2136. PMLR, 2018. [2](#)
- [17] Sarthak Jain and Byron C Wallace. Attention is not explanation. *arXiv preprint arXiv:1902.10186*, 2019. [2](#)
- [18] ME Kelly, A Heeney, CE Redmond, J Costelloe, GJ Nason, J Ryan, D Brophy, and DC Winter. Incidental findings detected on emergency abdominal ct scans: a 1-year review. *Abdominal imaging*, 40(6):1853–1857, 2015. [1](#)
- [19] Bastien Le Guellec, Alexandre Lefèvre, Charlotte Geay, Lucas Shorten, Cyril Brûge, Lotfi Hacine-Bey, Philippe Amouyel, Jean-Pierre Pruvo, Gregory Kuchinski, and Aghiles Hamroun. Performance of an open-source large language model in extracting information from free-text radiology reports. *Radiology: Artificial Intelligence*, 6(4):e230364, 2024. [1](#)
- [20] Hao-Chih Lee, Zelong Liu, Hamza Ahmed, Spencer Kim, Sean Huver, Vishwesh Nath, Zahi A Fayad, Timothy Deyer, and Xueyan Mei. Unified supervision for vision-language modeling in 3d computed tomography. *arXiv preprint arXiv:2509.01554*, 2025. [2](#) [5](#)

[21] Jingyang Lin, Yingda Xia, Jianpeng Zhang, Ke Yan, Le Lu, Jiebo Luo, and Ling Zhang. Ct-glip: 3d grounded language-image pretraining with ct scans and radiology reports for full-body scenarios. *arXiv preprint arXiv:2404.15272*, 2024. 1, 2, 3

[22] Che Liu, Yinda Chen, Haoyuan Shi, Jinpeng Lu, Bailiang Jian, Jiazen Pan, Linghan Cai, Jiayi Wang, Yundi Zhang, Jun Li, et al. Does dinov3 set a new medical vision standard? *arXiv preprint arXiv:2509.06467*, 2025. 1

[23] Zhuang Liu, Hanzi Mao, Chao-Yuan Wu, Christoph Feichtenhofer, Trevor Darrell, and Saining Xie. A convnet for the 2020s. In *Proceedings of the IEEE/CVF conference on computer vision and pattern recognition*, pages 11976–11986, 2022. 3

[24] Minh-Thang Luong, Hieu Pham, and Christopher D Manning. Effective approaches to attention-based neural machine translation. *arXiv preprint arXiv:1508.04025*, 2015. 2, 3

[25] Pritam Mukherjee, Benjamin Hou, Ricardo B Lanfredi, and Ronald M Summers. Feasibility of using the privacy-preserving large language model vicuna for labeling radiology reports. *Radiology*, 309(1):e231147, 2023. 1

[26] Organisation for Economic Co-operation and Development. Computed tomography (ct) exams. OECD Data Indicators, 2025. Accessed: 2025-10-29. 1

[27] Ali Pourvaziri, Anand K Narayan, David Tso, Vinit Baliyan, McKinley Glover IV, Bernardo C Bizzo, Bashar Kako, Marc D Succi, Michael H Lev, and Efren J Flores. Imaging information overload: Quantifying the burden of interpretive and non-interpretive tasks for computed tomography angiography for aortic pathologies in emergency radiology. *Current Problems in Diagnostic Radiology*, 51(4):546–551, 2022. 1

[28] Alec Radford, Jong Wook Kim, Chris Hallacy, Aditya Ramesh, Gabriel Goh, Sandhini Agarwal, Girish Sastry, Amanda Askell, Pamela Mishkin, Jack Clark, et al. Learning transferable visual models from natural language supervision. In *International conference on machine learning*, pages 8748–8763. PMLR, 2021. 1

[29] Daniel Reichenpfader, Henning Müller, and Kerstin Dencke. A scoping review of large language model based approaches for information extraction from radiology reports. *npj Digital Medicine*, 7(1):222, 2024. 1

[30] Alexander Ritter, Maximilian Sabev, Olivier Bonny, Greigoire Wuerzner, Thomas Ernandez, Florian Buchkremer, Stephan Segerer, Daniel G Fuster, Beat Roth, Nilufar Mohabbi, et al. Incidental findings on non-contrast abdominal computed tomography in an asymptomatic population: Prevalence, economic and health implications. *PLoS One*, 20(8):e0328049, 2025. 1

[31] Saikat Roy, Gregor Kochler, Constantin Ulrich, Michael Baumgartner, Jens Petersen, Fabian Isensee, Paul F Jaeger, and Klaus H Maier-Hein. Mednext: transformer-driven scaling of convnets for medical image segmentation. In *International Conference on Medical Image Computing and Computer-Assisted Intervention*, pages 405–415. Springer, 2023. 3

[32] Zhongyi Shui, Jianpeng Zhang, Weiwei Cao, Sinuo Wang, Ruizhe Guo, Le Lu, Lin Yang, Xianghua Ye, Tingbo Liang, Qi Zhang, et al. Large-scale and fine-grained vision-language pre-training for enhanced ct image understanding. *arXiv preprint arXiv:2501.14548*, 2025. 1, 2

[33] Siemens Healthineers. syngo.via — get the full picture. Siemens Healthineers USA. 1

[34] Oriane Siméoni, Huy V Vo, Maximilian Seitzer, Federico Baldassarre, Maxime Oquab, Cijo Jose, Vasil Khalidov, Marc Szafraniec, Seungeun Yi, Michaël Ramamonjisoa, et al. Dinov3. *arXiv preprint arXiv:2508.10104*, 2025. 1, 3

[35] Rebecca Smith-Bindman, Philip W Chu, Hana Azman Firdaus, Carly Stewart, Matthew Malekhdayan, Susan Alber, Wesley E Bolch, Malini Mahendra, Amy Berrington de González, and Diana L Miglioretti. Projected lifetime cancer risks from current computed tomography imaging. *JAMA internal medicine*, 185(6):710–719, 2025. 1

[36] Synopsys. Simpleware auto segmentation tools. Synopsys Simpleware. 1, 2

[37] Christian Szegedy, Wei Liu, Yangqing Jia, Pierre Sermanet, Scott Reed, Dragomir Anguelov, Dumitru Erhan, Vincent Vanhoucke, and Andrew Rabinovich. Going deeper with convolutions. In *Proceedings of the IEEE conference on computer vision and pattern recognition*, pages 1–9, 2015. 1

[38] Hugo Touvron, Thibaut Lavril, Gautier Izacard, Xavier Martinet, Marie-Anne Lachaux, Timothée Lacroix, Baptiste Rozière, Naman Goyal, Eric Hambro, Faisal Azhar, et al. Llama: Open and efficient foundation language models. *arXiv preprint arXiv:2302.13971*, 2023. 1

[39] Fakrul Islam Tushar, Vincent M D’Anniballe, Rui Hou, Maciej A Mazurowski, Wanyi Fu, Ehsan Samei, Geoffrey D Rubin, and Joseph Y Lo. Classification of multiple diseases on body ct scans using weakly supervised deep learning. *Radiology: Artificial Intelligence*, 4(1):e210026, 2021. 2

[40] Ashish Vaswani, Noam Shazeer, Niki Parmar, Jakob Uszkoreit, Llion Jones, Aidan N Gomez, Łukasz Kaiser, and Illia Polosukhin. Attention is all you need. *Advances in neural information processing systems*, 30, 2017. 1, 2, 3

[41] Jan Vossenrich, Philipp Brantner, Joshy Cyriac, Daniel T Boll, Elmar M Merkle, and Tobias Heye. Quantifying radiology resident fatigue: analysis of preliminary reports. *Radiology*, 298(3):632–639, 2021. 1

[42] Tassilo Wald, Ibrahim Ethem Hamamci, Yuan Gao, Sam Bond-Taylor, Harshita Sharma, Maximilian Ilse, Cynthia Lo, Olesya Melnichenko, Noel CF Codella, Maria Teodora Wetscherek, et al. Comprehensive language-image pre-training for 3d medical image understanding. *arXiv preprint arXiv:2510.15042*, 2025. 2, 6

[43] Xiaolong Wang, Ross Girshick, Abhinav Gupta, and Kaiming He. Non-local neural networks. In *Proceedings of the IEEE conference on computer vision and pattern recognition*, pages 7794–7803, 2018. 2, 3

[44] Jakob Wasserthal, Hanns-Christian Breit, Manfred T Meyer, Maurice Pradella, Daniel Hinck, Alexander W Sauter, Tobias Heye, Daniel T Boll, Joshy Cyriac, Shan Yang, et al. Totalsegmentator: robust segmentation of 104 anatomic structures in ct images. *Radiology: Artificial Intelligence*, 5(5):e230024, 2023. 1, 2, 5

- [45] M Winder, AJ Owczarek, J Chudek, J Pilch-Kowalczyk, and J Baron. Are we overdoing it? changes in diagnostic imaging workload during the years 2010-2020 including the impact of the sars-cov-2 pandemic. *healthcare (basel)*, 2021. [1](#)
- [46] Kelvin Xu, Jimmy Ba, Ryan Kiros, Kyunghyun Cho, Aaron Courville, Ruslan Salakhudinov, Rich Zemel, and Yoshua Bengio. Show, attend and tell: Neural image caption generation with visual attention. In *International conference on machine learning*, pages 2048–2057. PMLR, 2015. [2](#), [3](#)
- [47] Manzil Zaheer, Satwik Kottur, Siamak Ravanbakhsh, Barnabas Poczos, Russ R Salakhutdinov, and Alexander J Smola. Deep sets. *Advances in neural information processing systems*, 30, 2017. [2](#)
- [48] Xiaohua Zhai, Basil Mustafa, Alexander Kolesnikov, and Lucas Beyer. Sigmoid loss for language image pre-training. In *Proceedings of the IEEE/CVF international conference on computer vision*, pages 11975–11986, 2023. [3](#)

Organ-Aware Attention Improves CT Triage and Classification
Supplementary Material

Table of Contents

A. Data & Preprocessing	3
A.1 CT-RATE organ merges (table)	3
A.2 MERLIN organ merges (table)	4
A.3 CT-RATE vs RAD-ChestCT prevalence (fig)	3
A.4 MERLIN class prevalence (fig)	5
B. Results	6
B.1 Chest	6
B.1.1 Chest Model Heatmaps	6
B.1.2 CT-RATE (four modes)	7
B.1.3 RAD-ChestCT (four modes)	7
B.2 Abdomen	8
B.2.1 Merlin Models Comparison AUROC/AUPRC [Scalar=Mask]	8
B.2.2 Merlin Model - DINOV3 Mode Comparison AUROC/AUPRC [Scalar=Mask]	9
C. Ablations	10
C.1 Merlin Backbone: frozen vs. unfrozen (GAP)	10
C.2 Merlin Scalars (Mask fixed): HU vs. Vol	11
C.3 Merlin Region: Mask vs. BBox	12
D. Training & Evaluation Details	13
D.1 Shared training setup (table)	13
D.2 Augmentation presets (table)	13
D.3 Model-specific deltas (table)	13
D.4 Zero-shot prompts — MERLIN (table)	14
E. ORACLE-CT with Dinov3 Implementation Notes	15

Table 7. **CT-RATE (chest):** TotalSegmentator classes → merged organ groups → dilation (mm) → mapped disease labels.

TotalSegmentator classes	Merged organ group	Dilation (mm)	Mapped disease labels
lung_upper_lobe_left, lung_lower_lobe_left, lung_upper_lobe_right, lung_middle_lobe_right, lung_lower_lobe_right	lung	2.0	Emphysema, Atelectasis, Lung nodule, Lung opacity, Pulmonary fibrotic sequela, Pleural effusion, Mosaic attenuation pattern, Peribronchial thickening, Consolidation, Bronchiectasis, Interlobular septal thickening
heart, atrial_appendage_left Coronary artery wall calcification	heart	2.0	Cardiomegaly, Pericardial effusion,
stomach, esophagus	stomach_esophagus	1.0	Hiatal hernia
aorta	aorta	2.0	Arterial wall calcification
—	other	—	Medical material, Lymphadenopathy

Note: **other** conditions are not mapped to any organ mask (no consistent organ-localized mask available) and are predicted by a global head without organ masking. Dilation values are metric-space dilations applied to masks prior to pooling.

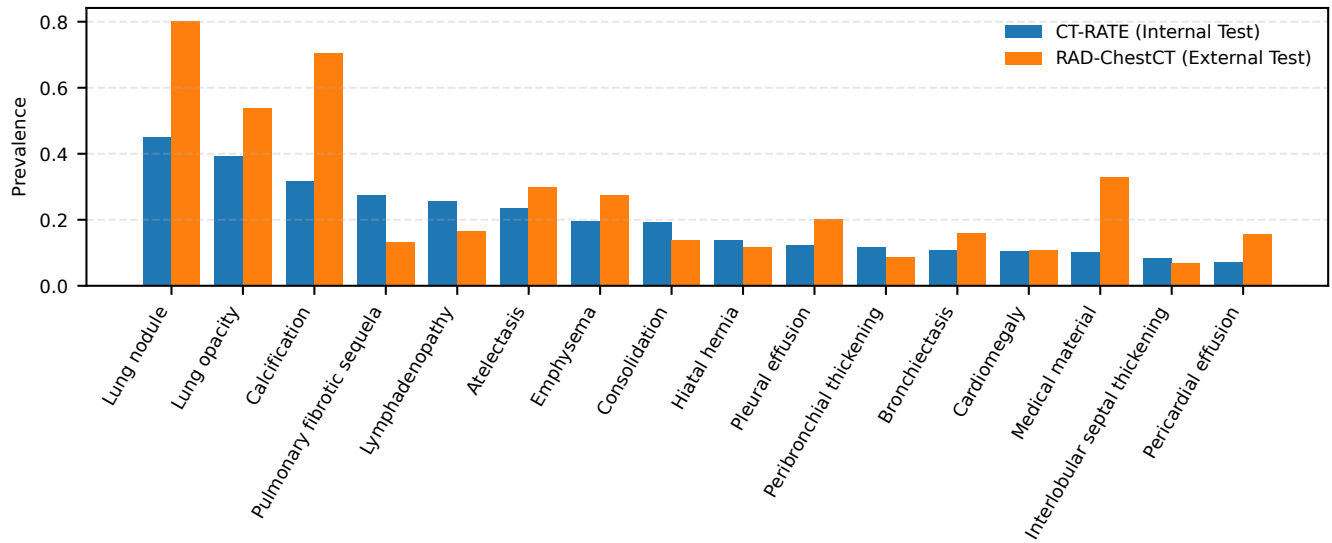


Figure 4. Prevalence comparison on the **harmonized 16-label chest space**. Bars show per-label prevalence in **CT-RATE (Internal Test)** and **RAD-ChestCT (External Test)**, ordered by CT-RATE prevalence. For visualization, CT-RATE *Calcification* is computed as the union of *Arterial wall calcification* and *Coronary artery wall calcification*, and *Mosaic attenuation pattern* is excluded because it is not annotated in RAD-ChestCT.

Table 8. **MERLIN (abdomen):** TotalSegmentator classes → merged organ groups → dilation (mm) → mapped disease labels.

TotalSegmentator classes	Merged organ group	Dilation (mm)	Mapped disease labels
liver	liver	3.0	Hepatic steatosis, Hepatomegaly, Biliary ductal dilation
gallbladder	gallbladder	4.0	Gallstones, Surgically absent gallbladder
pancreas	pancreas	2.0	Pancreatic atrophy
spleen	spleen	3.0	Splenomegaly
kidney_left, kidney_right	kidneys	5.0	Hydronephrosis, Renal cyst, Renal hypodensities
prostate	prostate	4.0	Prostatomegaly
stomach, esophagus	stomach_esophagus	3.0	Hiatal hernia
small_bowel, duodenum, colon	bowel	3.0	Appendicitis, Bowel obstruction, Submucosal edema
lung_upper_lobe_left, lung_lower_lobe_left, lung_upper_lobe_right, lung_middle_lobe_right, lung_lower_lobe_right	lungs	3.0	Atelectasis, Pleural effusion
heart, atrial_appendage_left	heart	4.0	Cardiomegaly, Coronary calcification, Aortic valve calcification
aorta, brachiocephalic_trunk, arteries subclavian_artery L/R, common_carotid_artery L/R, iliac_artery L/R		3.0	Abdominal aortic aneurysm, Atherosclerosis
inferior_vena_cava, superior_vena_cava, portal_vein_and_splenic_vein, iliac_vein L/R, brachiocephalic_vein L/R, pulmonary_vein	veins	3.0	Thrombosis
Vertebrae C1--S1, ribs L/R 1--12, sacrum, sternum, clavicles L/R, scapula L/R, hips L/R, femur L/R, humerus L/R, skull	bones	0.5	Osteopenia, Fracture
—	other	—	Anasarca, Ascites, Free air, Lymphadenopathy, Metastatic disease

Note: **other** conditions are not mapped to any organ mask (no consistent organ-localized mask available) and are predicted by a global head without organ masking. Dilation values are metric-space dilations applied to masks prior to pooling.

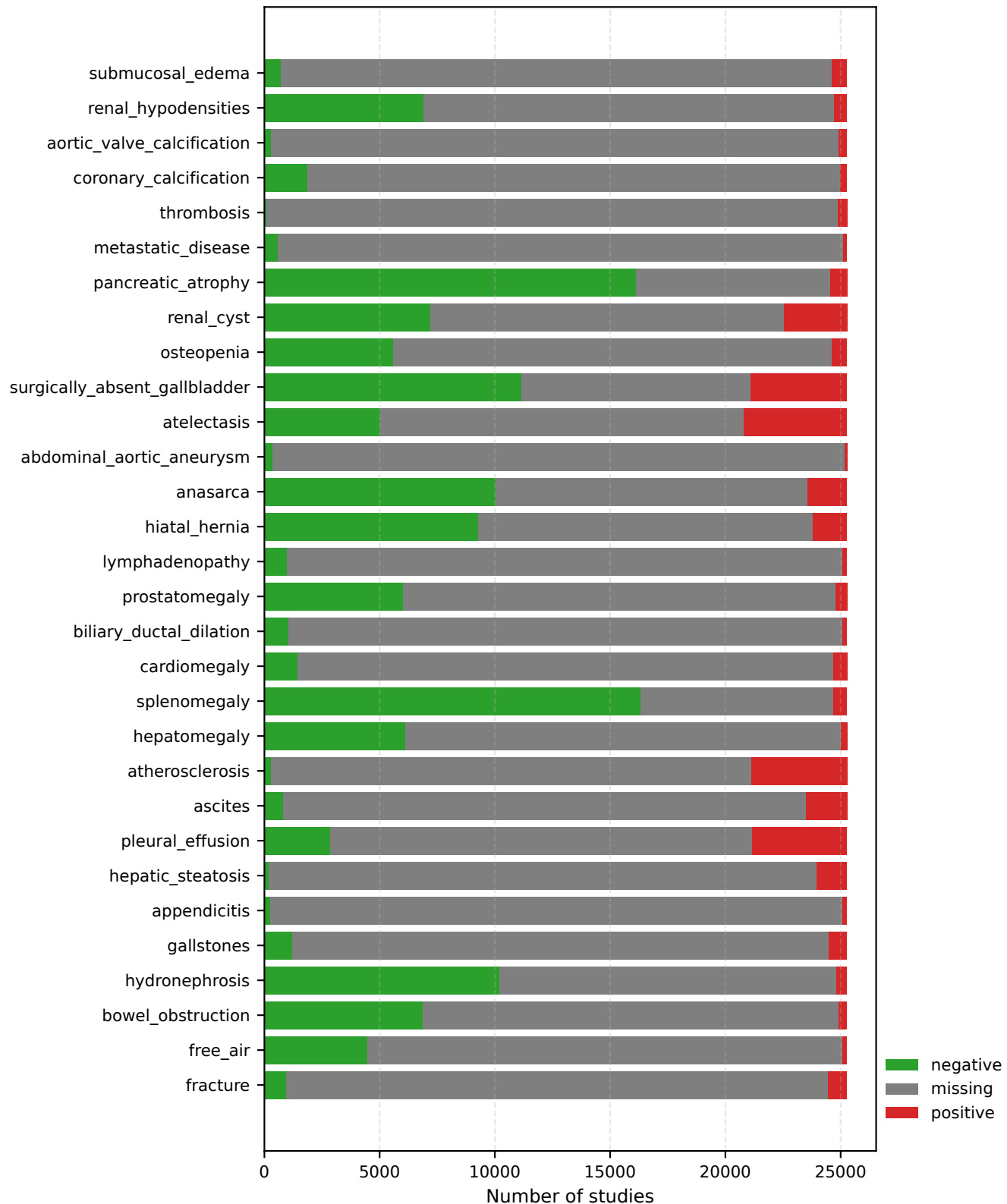


Figure 5. **MERLIN (abdomen) class prevalence.** Horizontal stacked bar plot showing, for each of the 30 findings (y-axis), the total number of studies (x-axis) partitioned into **negatives (0)**, **positives (1)**, and **uncertain/missing (-1)**. Counts are aggregated over MERLIN *train+val+test*.

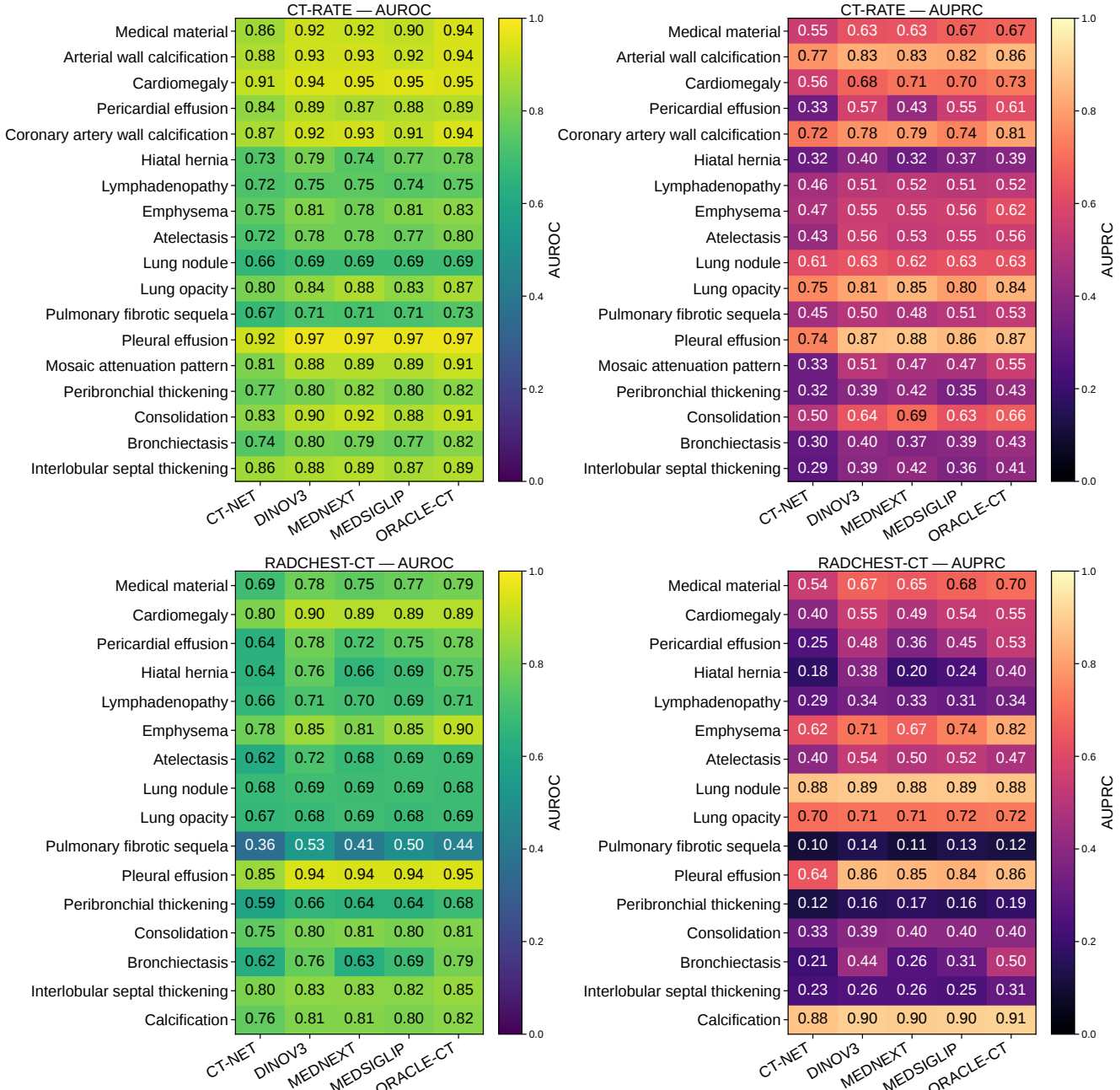


Figure 6. **Per-class AUROC and AUPRC heatmaps on CT-RATE (top) and RADChest-CT (bottom).** Left column shows AUROC; right column shows AUPRC. Rows are disease labels and columns are models (e.g., CT-NET, DINOV3, MEDNEXT, MEDSIGLIP, ORACLE-CT). Each cell prints the exact score, while color encodes magnitude using distinct, metric-specific colormaps (see colorbars).

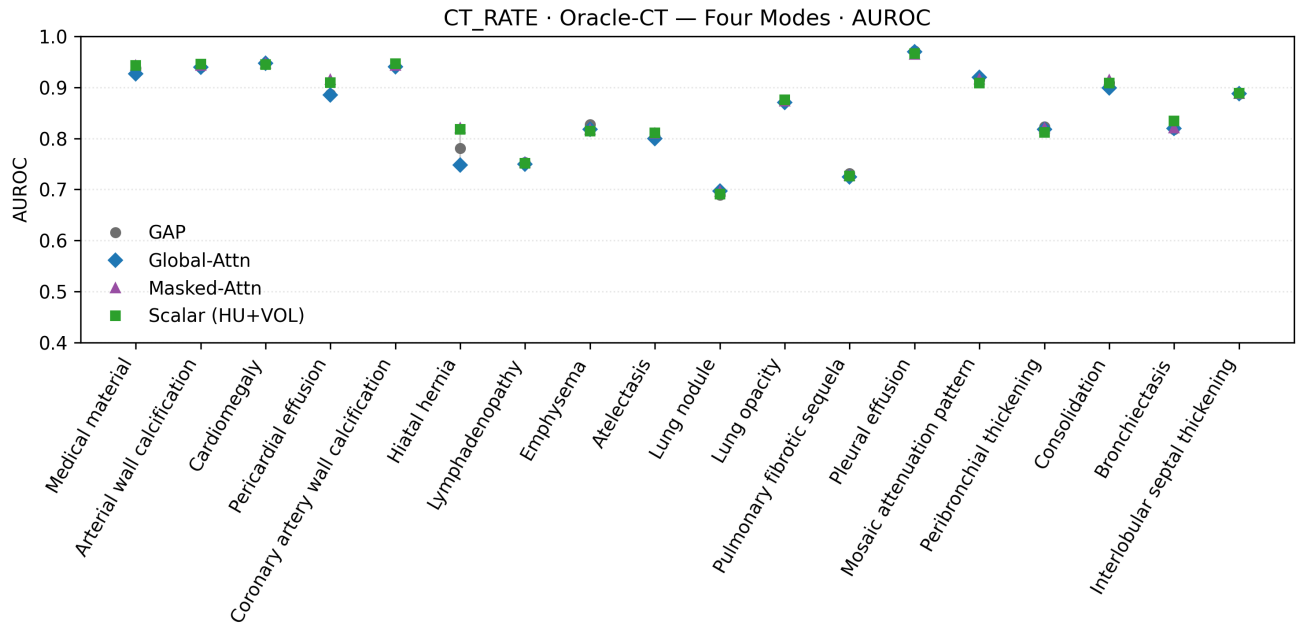


Figure 7. **CT-RATE, ORACLE-CT mode ablation (per-label).** Four modes (GAP, Global, Masked, Masked+Scalar) show tightly clustered performance; median differences are small, reflecting coarse chest anatomy.

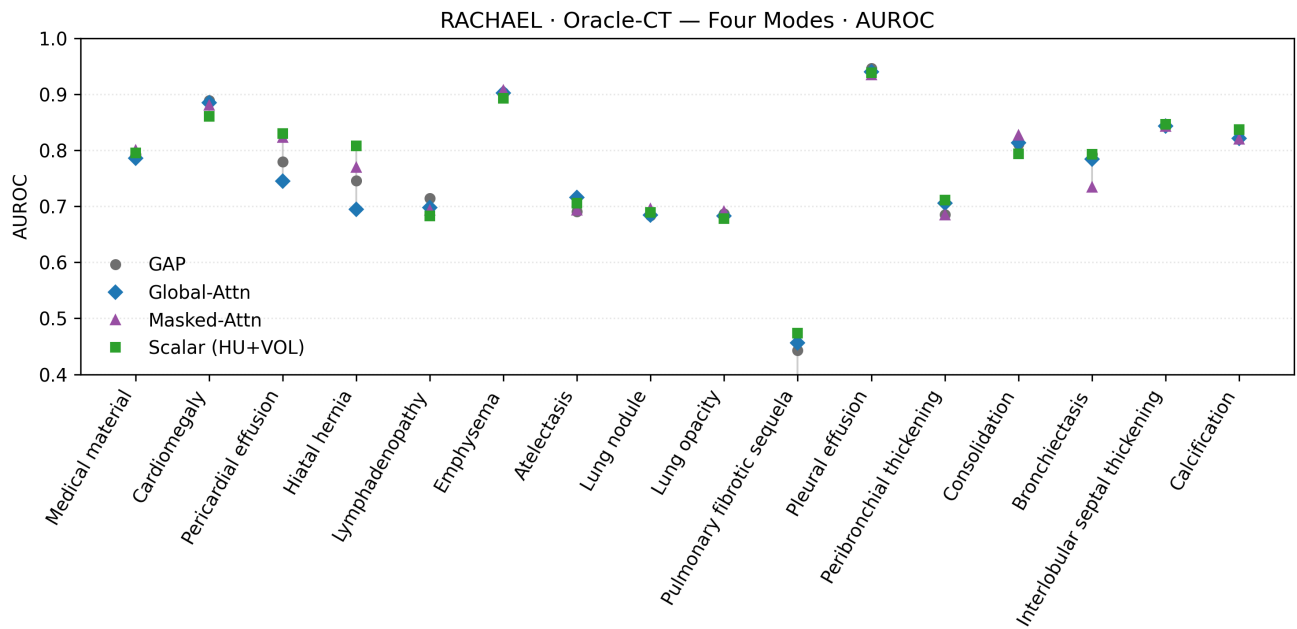


Figure 8. **RAD-ChestCT, ORACLE-CT mode ablation (per-label).** Four modes (GAP, Global, Masked, Masked+Scalar) show tightly clustered performance; median differences are small, reflecting coarse chest anatomy.

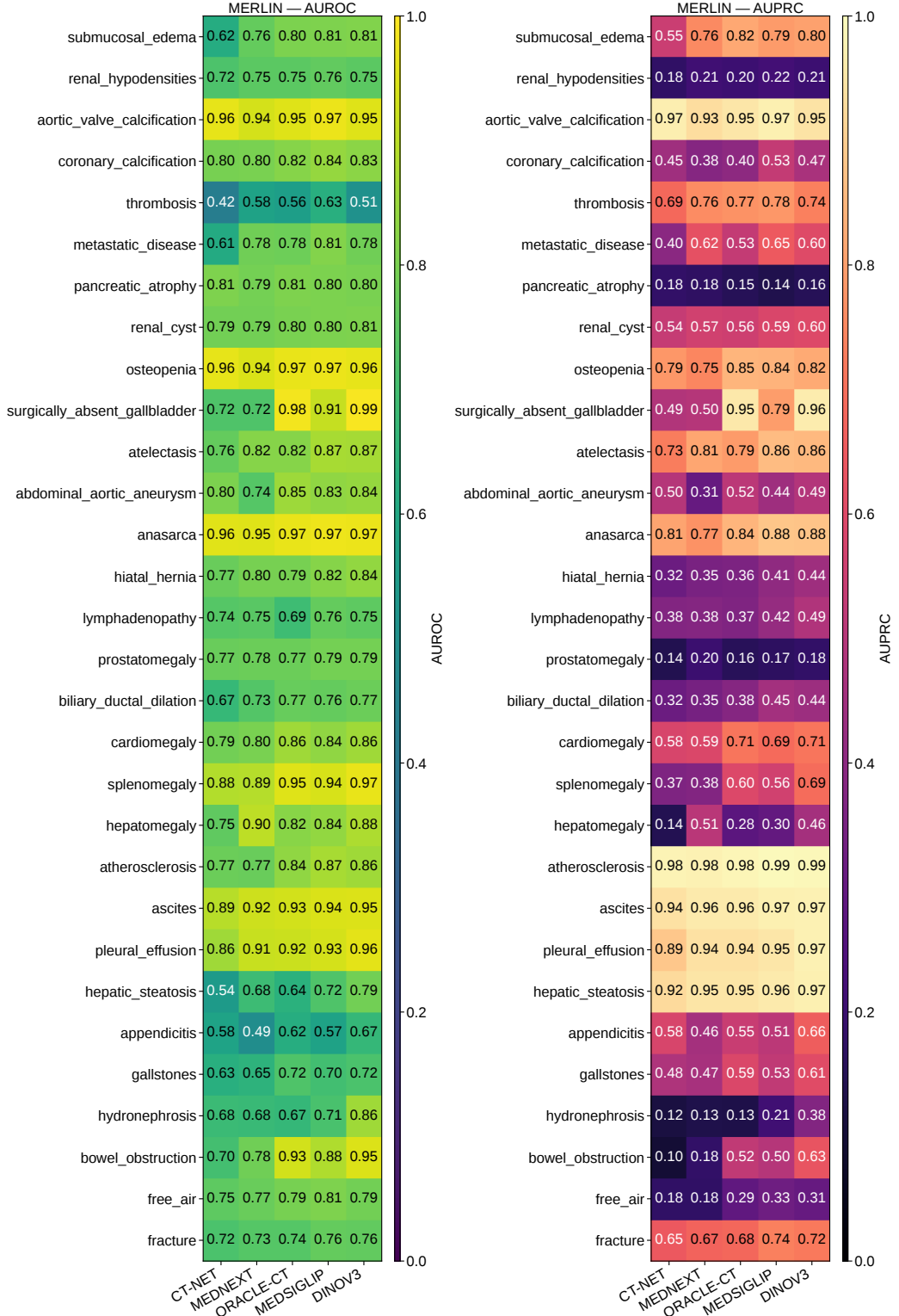


Figure 9. MERLIN test set — GAP baseline (Global Average Pooling). Per-class heatmaps compare five encoders with unfrozen backbones. *Left:* AUROC. *Right:* AUPRC. Columns (left→right): CT-NET, MEDNEXT, ORACLE-CT, MEDSIGLIP, DINOV3; rows are the 30 abdominal findings. Overall, DINOV3 and MEDSIGLIP lead across most classes, ORACLE-CT is competitive mid-pack, and MEDNEXT/CT-NET trail. High-signal targets (e.g., calcifications, pleural effusion, hepatic steatosis) approach saturation across models, while gaps are larger on lower-prevalence/acute findings (e.g., appendicitis, bowel obstruction, free air, gallstones).

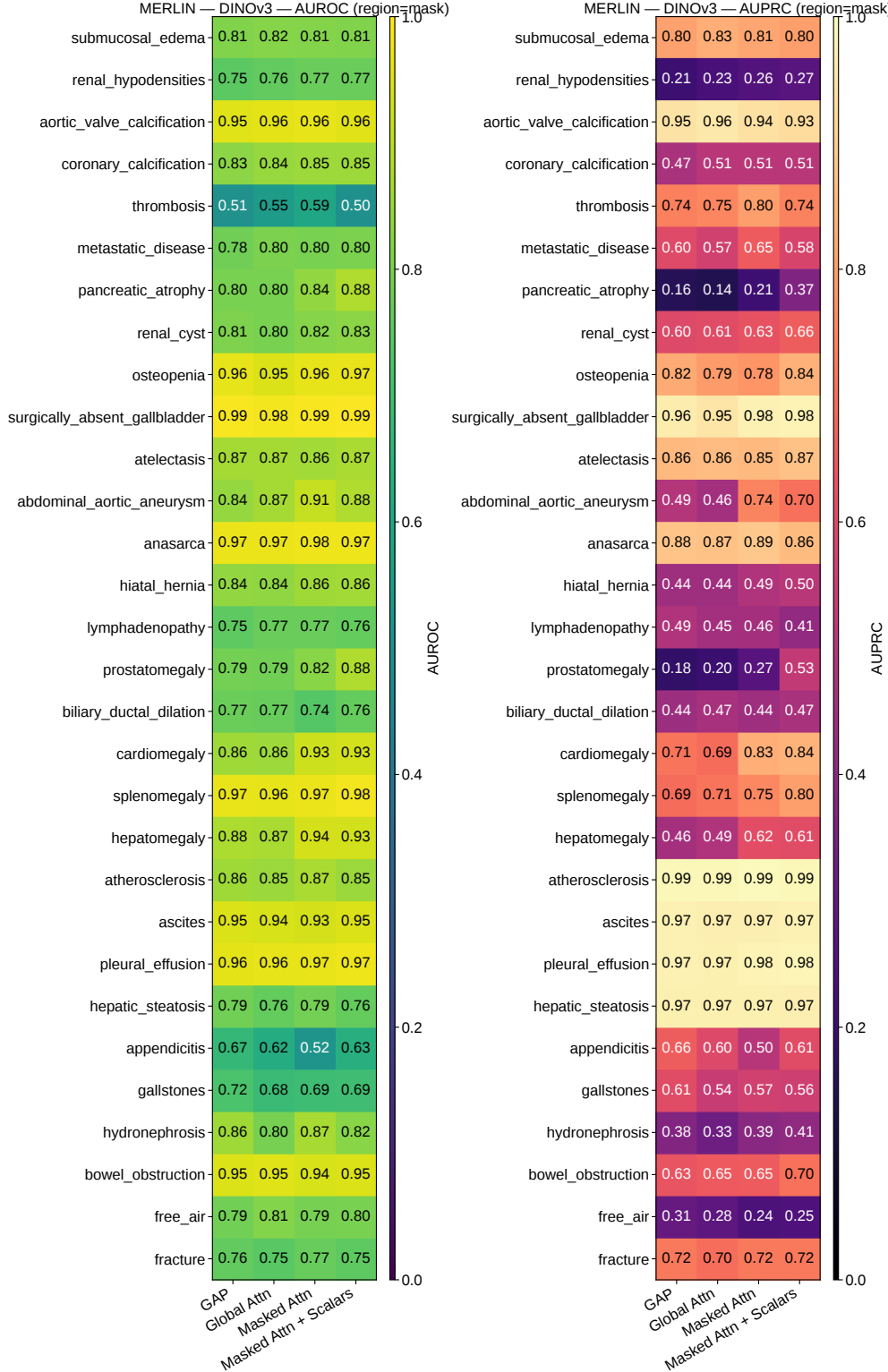


Figure 10. **DINOv3—Four aggregation modes with organ masks (AUROC/AUPRC, 30 MERLIN classes).** GAP (global average pooling baseline), *global_attn* (unconstrained token attention), *masked_attn* (attention restricted to the target organ using *mask_region=Mask*), and *masked_attn_scalar* (masked attention with scalar fusion of organ *volume* and mean *HU*). Columns enumerate the four modes; rows list the 30 abdominal labels. Brighter cells indicate higher AUROC. Organ-aware heads (*masked_attn* / *masked_attn_scalar*) confine evidence to anatomy and typically improve class-specific discrimination over GAP, with *masked_attn_scalar* adding small gains by injecting simple volumetric and intensity cues.

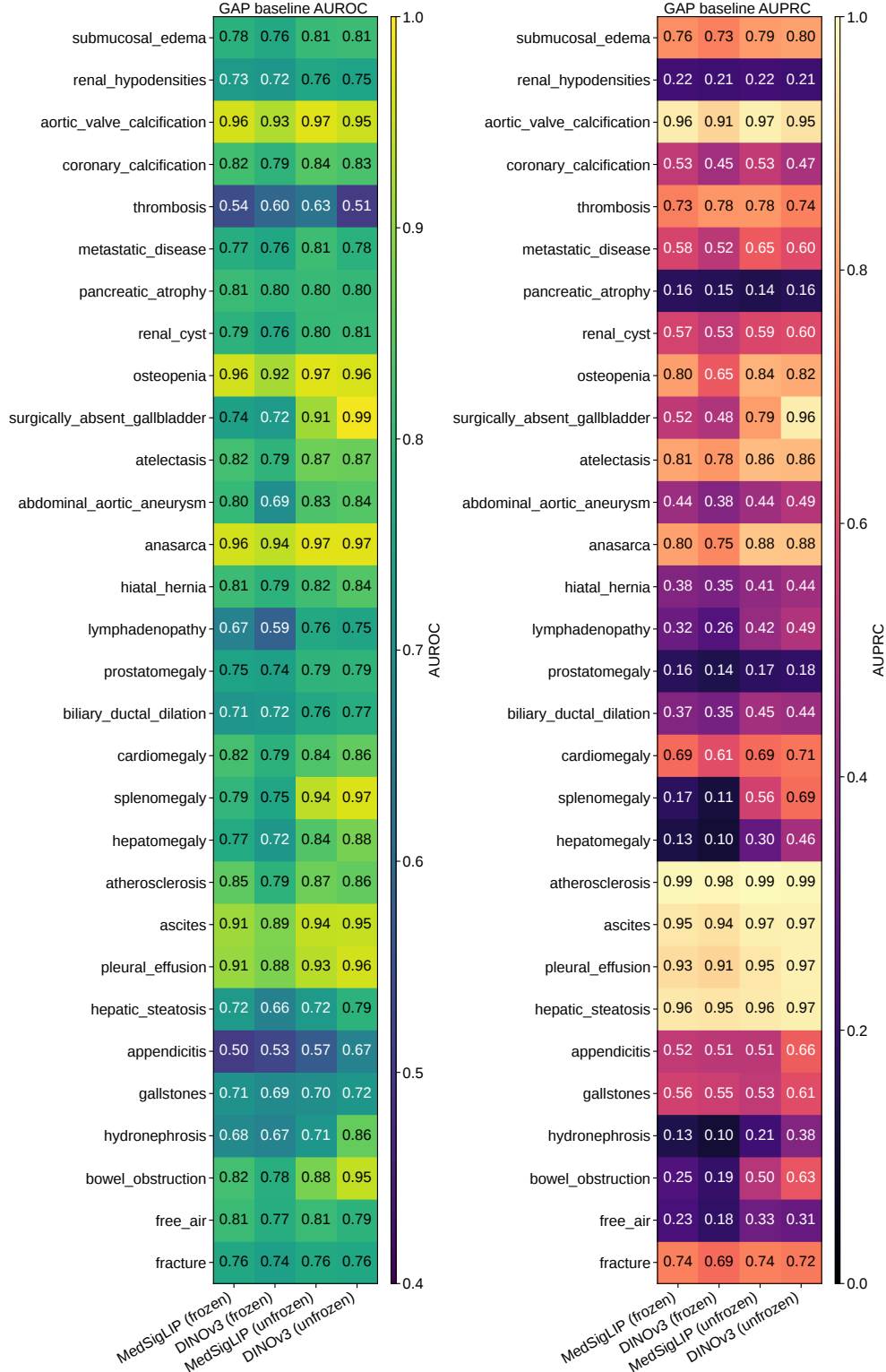


Figure 11. Backbone freeze vs. unfreeze (AUROC/AUPRC; GAP baseline; 30 MERLIN classes). Absolute per-class AUROC/AUPRC heatmaps for two encoders—DINOv3 and MedSigLIP—trained with a GAP head under two regimes: *frozen* backbone and *unfrozen* backbone. Columns enumerate (encoder \times freeze state); rows list the 30 abdominal labels. Unfreezing generally raises AUPRC, with the clearest gains on multi-organ and morphology/size-driven findings (e.g., spleno-/hepato-/cardiomegaly, bowel obstruction, surgically absent gallbladder). Highly localized or primarily HU-driven patterns (e.g., pancreatic atrophy, free air) change less, motivating the mask-region and scalar-fusion ablations that follow. Main results elsewhere use unfrozen backbones.

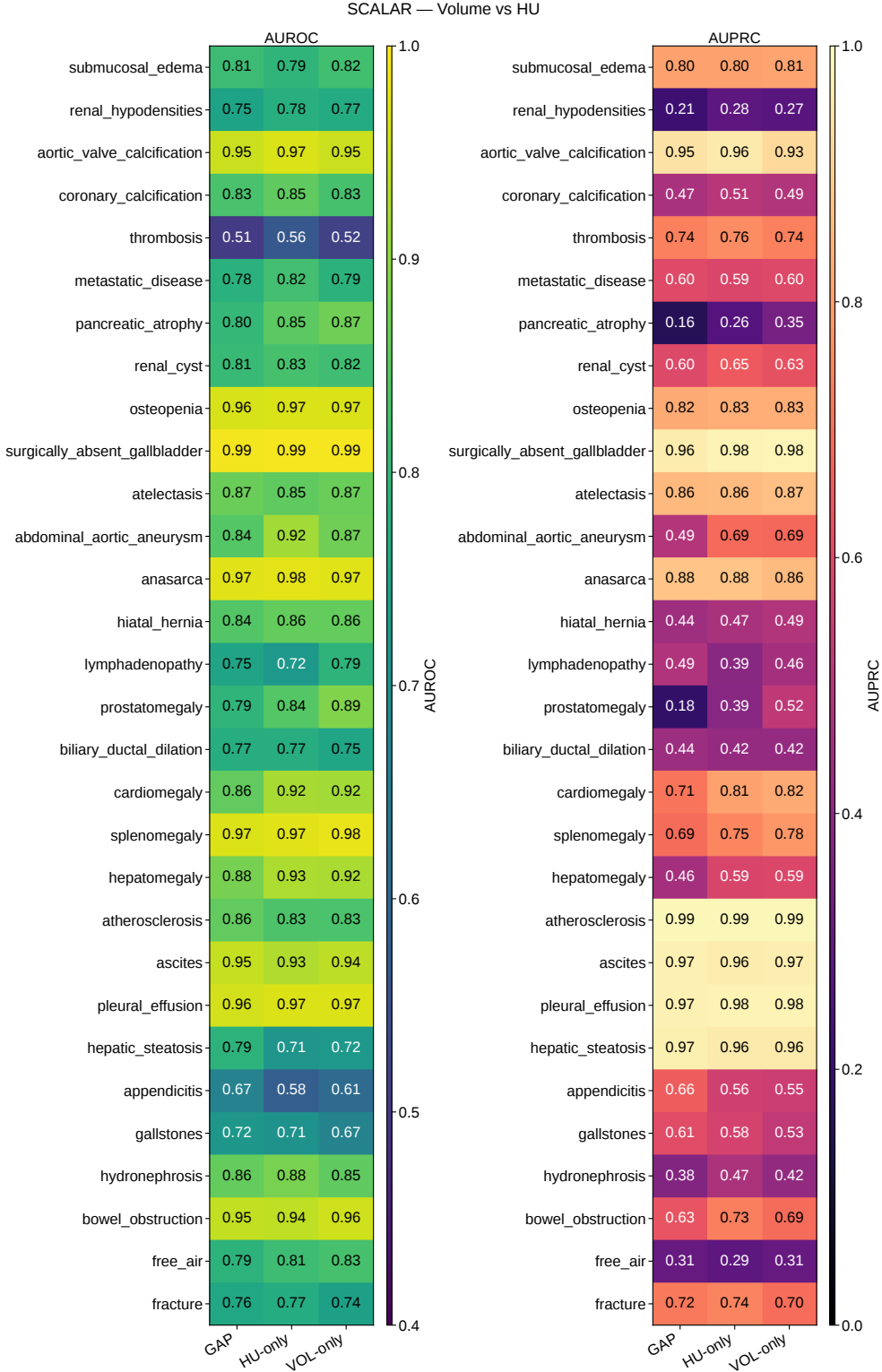


Figure 12. Scalar fusion ablation (absolute AUROC; mask region = Mask). Heatmap of per-class *absolute* AUROC/AUPRC under the *masked_attn_scalar* head with the region fixed to the full Segmentation Mask. Columns enumerate scalar variants—*HU-only* vs. *Volume-only*—trained with the same encoder and recipe; rows list the 30 MERLIN labels. Volume tends to aid morphology/size–driven findings *e.g.* cardio-/hepato-/splenomegaly, pancreatic atrophy), while HU favors intensity/density patterns (*e.g.*, calcifications, thrombosis). Both variants typically outperform the GAP baseline. Brighter cells indicate higher AUROC.

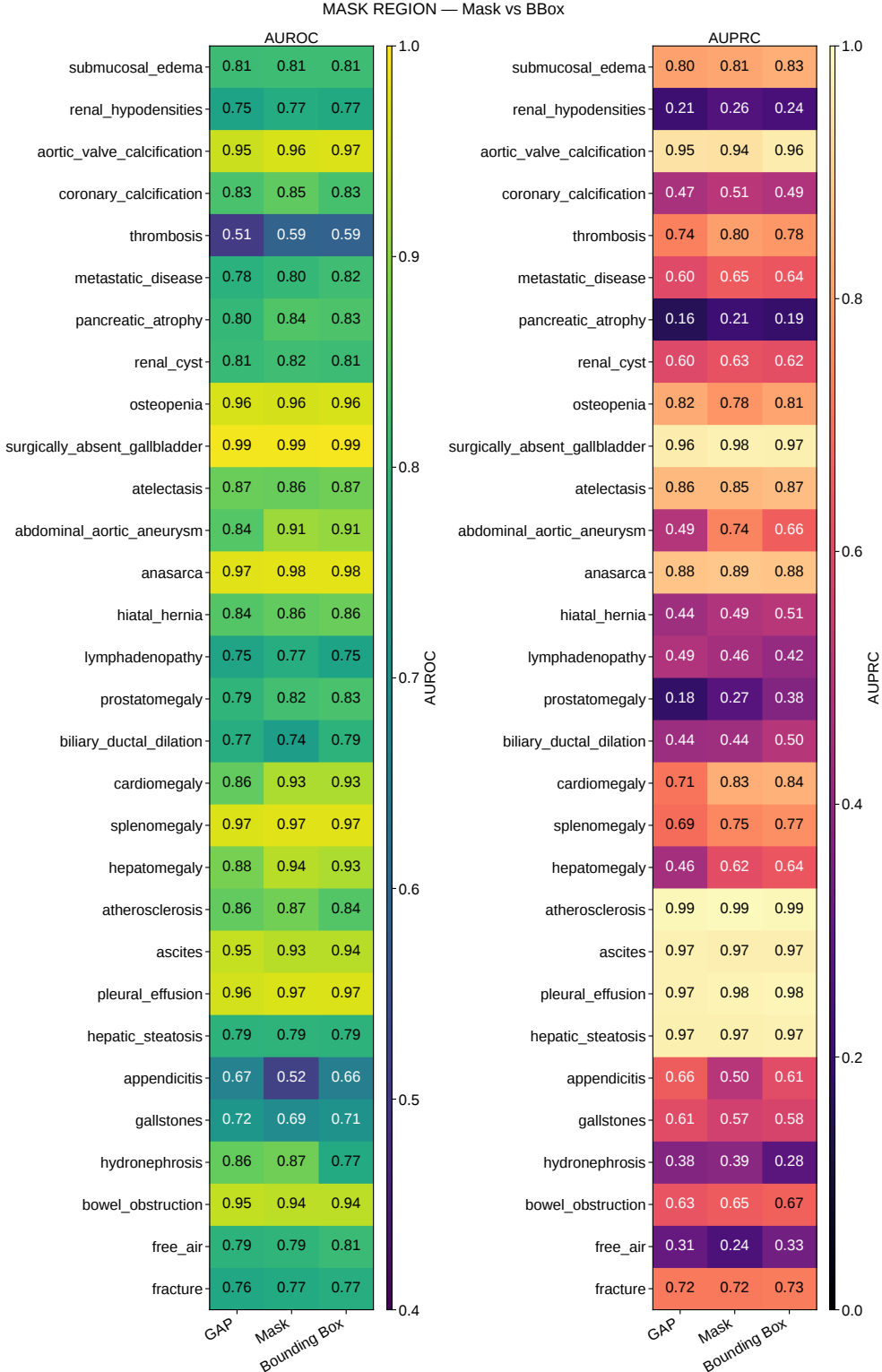


Figure 13. Mask region ablation - Mask vs Bounding Box (BBox). Heatmap of per-class *absolute* AUROC when the aggregation region for the organ-aware attention head is either the full Segmentation Mask or its tight Bounding Box. Columns enumerate region choice compared to GAP Baseline; rows list the 30 MERLIN labels. Both regions generally outperform the GAP baseline. The preferred region is class-dependent: e.g., *appendicitis* benefits from BBox, which better captures periappendiceal context (+26.92% AUROC; 0.66 vs. 0.52), and *biliary ductal dilation* gains from BBox that includes periportal/pancreatic-head context (+6.75%; 0.79 vs. 0.74). Brighter cells indicate higher AUROC.

Table 9. **Shared training configuration (all models).** Single run with fixed seed; dataset-specific augmentations are summarized in App. A. Items not listed are identical across datasets and encoders.

Item	Setting
Seed	25
Optimizer	AdamW (lr=0.001, weight_decay=0.05)
LR schedule	Cosine decay with 5-epoch warmup; step-based updates; minimum LR = $0.1 \times \text{base}$
Parameter groups	Head LR scale = 3.0; “alpha” params LR scale = 0.3; group LRs enabled
Epochs / Early stop	Max 30 epochs; early stopping on <i>validation loss</i> , patience = 10
Model selection	Best <i>validation loss</i> checkpoint (checkpoint_policy: best_only)
Loss	BCE-uncertain: ignore first 10 epochs; ramp 10 epochs; final uncertain weight = 0.3 (target 0)
Class weighting	Positive-class weighting enabled (use_pos_weight: true); clip at 10.0
Precision	Mixed precision (AMP)
Regularization	Global-norm grad clip = 1.0; attn_entropy_reg_weight = 0; attn_coverage_reg_weight = 0
Parallelism	Distributed Data Parallel (ddp: true); cudnn_benchmark: true
Logging	Log every 1000 steps
Transforms	Image/mask transforms applied jointly; masks resampled with nearest; border padding
Empty-mask fallback	Uniform pooling over Ω
Calibration	Per-label temperature scaling on validation (max_iter = 200, min_count = 64)
Thresholds	Validation F1-optima, transferred unchanged to test and external sets
Augmentations (by dataset)	CT-RATE: legacy_v1 ($k \times 90^\circ$ rotations; axis flips). MERLIN: anatomy_safe_v2 (small in-plane affine, mild gamma & noise; flips <i>disabled</i> to preserve laterality).

Table 10. Augmentation presets and parameters (applied to images and masks together).

Dataset	Preset	Parameters
CT-RATE	legacy_v1	allow_rot90: true, allow_flip_w: true, allow_flip_h: true, allow_flip_d: true
MERLIN	anatomy_safe_v2	p_affine: 0.35, rot_deg: 10.0, translate_xy: 5.0, scale_min: 0.95, scale_max: 1.05, allow_flip_w: false, allow_flip_h: false, allow_flip_d: false, p_gamma: 0.30, gamma_min: 0.90, gamma_max: 1.10, p_noise: 0.30, noise_std: 0.01

Table 11. Model-specific settings not shared across all encoders.

Model	Input size	Normalization	Freeze policy	Notes
DINOv3 (tokens)	$S \in \{224, 224\}$	ImageNet	trainable	TRI stride $s=1$
MedSigLIP (tokens)	$S=224$	CLIP	trainable	CLIP fallback norm
I3D-ResNet-121 (voxels)	224^3	[0-1]	trainable	stage 3/4 pooled
MedNeXt-3D (voxels)	$160 \times 224 \times 224$	[0-1]	trainable	optional pyramid
CT-Net (voxels)	$160 \times 224 \times 224$	[0-1]	trainable	light 3D neck

Table 12. **Zero-shot prompts used for *Merlin*.** We used these prompts with the released *Merlin* weights to reproduce zero-shot results on the *full* test split. Prompts were generated once with an LLM and fixed before evaluation.

Class	Positive prompt(s)	Negative prompt(s)
submucosal_edema	submucosal edema; bowel wall edema present	no submucosal edema; no bowel wall edema
renal_hypodensities	renal hypodensity; hypodense renal lesion	no renal hypodensity; no hypodense renal lesion
aortic_valve_calcification	aortic valve calcification present; calcified aortic valve	no aortic valve calcification
coronary_calcification	coronary artery calcifications; coronary calcification present	no coronary artery calcification; no coronary calcification
thrombosis	thrombosis; venous thrombosis; occlusive thrombus; nonocclusive thrombus	no thrombosis; no venous thrombus
metastatic_disease	metastatic disease; metastases present	no metastatic disease; no metastases
pancreatic_atrophy	pancreatic atrophy; atrophic pancreas	no pancreatic atrophy
renal_cyst	renal cyst; simple renal cyst	no renal cyst
osteopenia	osteopenia; low bone density	no osteopenia; normal bone mineralization
surgically_absent_gallbladder	surgically absent gallbladder; post cholecystectomy	gallbladder present; no prior cholecystectomy
atelectasis	atelectasis; subsegmental atelectasis	no atelectasis
abdominal_aortic_aneurysm	abdominal aortic aneurysm; infrarenal AAA	no abdominal aortic aneurysm
anasarca	anasarca; diffuse body wall edema	no anasarca; no diffuse body wall edema
hiatal_hernia	hiatal hernia	no hiatal hernia
lymphadenopathy	lymphadenopathy; enlarged lymph nodes	no lymphadenopathy; no enlarged lymph nodes
prostatomegaly	prostatomegaly; enlarged prostate	no prostatomegaly; prostate normal in size
biliary_ductal_dilation	biliary ductal dilatation; dilated bile ducts; intrahepatic biliary dilatation	no biliary ductal dilatation; bile ducts normal caliber
cardiomegaly	cardiomegaly; enlarged heart	no cardiomegaly
splenomegaly	splenomegaly; enlarged spleen	no splenomegaly
hepatomegaly	hepatomegaly; enlarged liver	no hepatomegaly
atherosclerosis	atherosclerosis; atherosclerotic calcifications	no atherosclerosis; no vascular calcification
ascites	ascites; free intraperitoneal fluid	no ascites; no free intraperitoneal fluid
pleural_effusion	pleural effusion; left pleural effusion; right pleural effusion	no pleural effusion
hepatic_steatosis	hepatic steatosis; fatty liver	no hepatic steatosis; no fatty liver
appendicitis	appendicitis; inflamed appendix	no appendicitis; normal appendix
gallstones	gallstones; cholelithiasis	no gallstones; no cholelithiasis
hydronephrosis	hydronephrosis; pelvicaliectasis	no hydronephrosis; no pelvicaliectasis
bowel_obstruction	bowel obstruction; small bowel obstruction	no bowel obstruction
free_air	free air; pneumoperitoneum	no free air; no pneumoperitoneum
fracture	fracture; vertebral fracture; rib fracture	no fracture; no acute fracture

6.1. ORACLE-CT with DINOV3 backbone

We detail ORACLE-CT on a 2.5D DINOV3 token tower (*Family A* in Sec. 3.2), while preserving the encoder-agnostic aggregation interface in Sec. 3.3.

TRI construction. Given a CT study $X \in \mathbb{R}^{D \times H \times W}$ (axial index first), choose a stride $s \in \mathbb{N}$ and centers $\mathcal{C} = \{c_t\}_{t=1}^T$ with

$$c_t = c_1 + s(t-1), \quad t = 1, \dots, T. \quad (8)$$

Define the tri-slice operator

$$\text{Tri}(X; c) = \text{stack}_{k=-1}^1 X_{c+k, :, :} \in \mathbb{R}^{3 \times H \times W}. \quad (9)$$

The per-study TRI sequence is

$$\mathbf{X}^{\text{TRI}} := (\text{Tri}(X; c_t))_{t=1}^T \in \mathbb{R}^{T \times 3 \times H \times W}. \quad (10)$$

Preprocessing. Each TRI slice is resized to $S \times S$ and channelwise normalized (DINOV3/ImageNet). Let \mathcal{P}_S denote this map. For a study and for a batch:

$$(\mathcal{P}_S(\text{Tri}(X; c_t)))_{t=1}^T \in \mathbb{R}^{T \times 3 \times S \times S}, \\ \mathbf{X}_S^{\text{TRI}} \in \mathbb{R}^{B \times T \times 3 \times S \times S}. \quad (11)$$

Patch tokenization and token lattice. Non-overlapping $P \times P$ patches on $S \times S$ yield a $g \times g$ grid with

$$g = S/P, \quad N = g^2. \quad (12)$$

We merge (B, T) to run slices independently through the ViT, drop non-spatial tokens, and unmerge:

$$\widehat{\mathbf{X}}_S^{\text{TRI}} := \text{merge}_{(B, T)}(\mathbf{X}_S^{\text{TRI}}) \in \mathbb{R}^{(BT) \times 3 \times S \times S}, \quad (13)$$

$$H = \text{ViT}(\widehat{\mathbf{X}}_S^{\text{TRI}}) \in \mathbb{R}^{(BT) \times (1+N+R) \times d}, \quad (14)$$

$$U = H[:, 1:1+N, :] \in \mathbb{R}^{(BT) \times N \times d}, \quad (15)$$

$$\mathbf{U} := \text{unmerge}_{(B, T)}(U) \in \mathbb{R}^{B \times T \times N \times d}. \quad (16)$$

Let the *token lattice* be the index set

$$\Omega = \{1, \dots, T\} \times \{1, \dots, N\}, \quad |\Omega| = TN.$$

We flatten $(t, p) \mapsto i$ via a fixed bijection $\iota : \{1, \dots, |\Omega|\} \leftrightarrow \Omega$ and write

$$u_i \equiv u_{t,p} \in \mathbb{R}^d \quad \text{for} \quad \iota(i) = (t, p).$$

All aggregation heads operate *only* on $\{u_i\}_{i \in \Omega}$, matching Sec. 3.3.

6.2. Organ mask projection to tokens (flattened i)

3D masks and per-slice extraction. Organ-group masks on the CT grid are

$$M_o \in \{0, 1\}^{D \times H \times W}, \quad o \in \mathcal{O}. \quad (17)$$

For a TRI center c_t , extract the axial slice (after any mm-dilation/padding specified in App. Tables 7 and 8):

$$\tilde{M}_{o,t} := M_o[c_t, :, :] \in \{0, 1\}^{H \times W}. \quad (18)$$

Projection to the patch grid and flattening. Masks reuse the image geometry: NN resize to $S \times S$, then NN down to the $g \times g$ patch grid

$$\Pi_{\text{patch}} := \text{NN}_{S \times S \rightarrow g \times g} \circ \text{NN}_{H \times W \rightarrow S \times S}, \quad (19)$$

yielding $\tilde{M}_{o,t}^{\text{patch}} \in \{0, 1\}^{g \times g}$. Flatten in the same raster order used by tokens to obtain binary indicators over the token lattice:

$$m_{o,i} \in \{0, 1\}, \quad m_{o,i} = 1 \Leftrightarrow \text{token } i \text{ lies in organ } o. \quad (20)$$

Let $\Omega_o = \{i \in \Omega : m_{o,i} = 1\}$ denote the support at the token resolution.

6.3. Aggregation modes with DINOV3 tokens (single index i)

All heads here use only $\{u_i\}_{i \in \Omega}$. Per-location scorers are *unary*

$$s : \mathbb{R}^d \rightarrow \mathbb{R} \quad (\text{Linear } (d \rightarrow 1) \text{ on tokens; no Q/K/V}). \quad (21)$$

(i) GAP baseline (uniform).

$$h = \frac{1}{|\Omega|} \sum_{i \in \Omega} u_i \in \mathbb{R}^d, \quad (22)$$

$$z = W^{\text{global}} h + b^{\text{global}} \in \mathbb{R}^L. \quad (23)$$

(ii) Global attention (mask-free).

$$\alpha_i = s_{\text{glob}}(u_i), \quad (24)$$

$$w_i = \frac{\exp(\alpha_i / \tau)}{\sum_{j \in \Omega} \exp(\alpha_j / \tau)}, \quad \tau > 0, \quad (25)$$

$$h = \sum_{i \in \Omega} w_i u_i, \quad z = W^{\text{global}} h + b^{\text{global}}. \quad (26)$$

(iii) Organ-masked attention. Each organ o has a scorer s_o , temperature $\tau_o > 0$, and optional priors $(\beta_o^{\text{in}}, \beta_o^{\text{out}})$:

$$\tilde{\alpha}_{o,i} = s_o(u_i) + \beta_o^{\text{in}} m_{o,i} + \beta_o^{\text{out}} (1 - m_{o,i}), \quad (27)$$

$$w_{o,i} = \frac{\exp(\tilde{\alpha}_{o,i} / \tau_o) m_{o,i}}{\sum_{j \in \Omega_o} \exp(\tilde{\alpha}_{o,j} / \tau_o) + \varepsilon}, \quad \varepsilon > 0, \quad (28)$$

$$h_o = \sum_{i \in \Omega_o} w_{o,i} u_i, \quad z_o = W^{(o)} h_o + b^{(o)} \in \mathbb{R}^{|\mathcal{L}_o|}. \quad (29)$$

If $\Omega_o = \emptyset$ at this resolution, we fall back to uniform pooling over Ω for that organ. Labels in $\mathcal{L}_{\text{other}}$ use the mask-free global head.

(iv) Organ-masked + scalar fusion (OSF). Compute per-organ scalars $u_o \in \mathbb{R}^k$ once from (dilated) masks (e.g., normalized volume, mean HU, border-contact flag). Let $b_o \in \{0, 1\}$ be the border flag and $g_o = \sigma(\gamma_o)$ a learned gate:

$$\tilde{h}_o = (1 - g_o b_o) h_o, \quad (30)$$

$$\hat{h}_o = [\tilde{h}_o; u_o] \in \mathbb{R}^{d+k}, \quad (31)$$

$$z_o = \text{MLP}_o(\hat{h}_o) \in \mathbb{R}^{|\mathcal{L}_o|}. \quad (32)$$

Finally, assemble $z \in \mathbb{R}^L$ by stitching $\{z_o\}$ with the fixed label→organ map.

Notes. (i) Temperatures (τ, τ_o) and priors $(\beta_o^{\text{in}}, \beta_o^{\text{out}})$ can be fixed or learned (we use learnable logits). (ii) (28) reduces to global attention when $m_{o,i} \equiv 1$. (iii) The same equations apply to voxel backbones by reinterpreting i as a flattened voxel index; only mask-to-lattice alignment changes.